EES Batteries

REVIEW

View Article Online
View Journal

Cite this: DOI: 10.1039/d5eb00156k

Three-dimensional lithium metal anodes in solid-state batteries

Chunting Wang,[a,b] Ruiguo Cao, [c] Jianbin Zhou*[a] and Shuhong Jiao *[a,d]

All-solid-state lithium-metal batteries (ASSLBs) are promising next-generation high-energy-density energy conversion and storage devices which leverage the high theoretical capacity of lithium metal anodes (LMAs) and nonflammable solid-state electrolytes (SSEs). However, uncontrolled dendrite propagation, substantial volume fluctuations, and interfacial void formation have severely compromised the interfacial contact integrity and impeded the practical applications of LMAs in solid-state batteries. The strategic incorporation of three-dimensional (3D) host matrices has emerged as a multifaceted solution to these interconnected challenges. This review systematically outlines contemporary advances in 3D LMA development, encompassing design principles, fabrication methodologies, and matrix material selection, providing critical perspectives on future research directions for ASSLBs applications.

Received 31st August 2025,
Accepted 25th November 2025

DOI: 10.1039/d5eb00156k

rsc.li/EESBatteries

Broader context

All-solid-state lithium metal batteries (ASSLBs) represent an emerging technology that employs solid-state electrolytes to replace conventional liquid-state electrolytes, thereby enhancing the safety, stability, and cycle life of energy storage systems. Developing stable lithium metal anodes (LMAs) is central to this evolution, yet remains a critical challenge due to uncontrolled dendrite propagation and interfacial degradation in ASSLBs. Three-dimensional (3D) Li-host architectures have emerged as a transformative strategy to spatially regulate Li deposition, enhance mechanical integrity, and prolong the cycle life. Unlike conventional planar anodes, 3D frameworks offer an expanded surface area, reduced local current density, and continuous ion pathways, collectively mitigating failure mechanisms intrinsic to ASSLBs. Centering on 3D LMAs, this review analyzes battery failure mechanisms to detail the strategies, methods, and advances and concludes with a discussion on prospective research paths for developing high performance ASSLBs.

1. Introduction

The application of high energy density batteries has gained significant traction across multiple advanced technological fields such as electrical vehicles, portable devices, aerospace engineering, medical devices, and advanced intelligent manufacturing systems.[1–4] Among various candidates, lithium metal batteries (LMBs) stand out with exceptional electrochemical characteristics, including an ultrahigh theoretical capacity of 3860 mAh g^{-1} and the lowest recorded redox potential (−3.04 V *vs.* SHE), positioning them as indispensable components for next-generation high-energy-density battery systems.[5] Nevertheless, the thermodynamic instability and mechanical instability of LMAs during operation induce severe safety concerns, including internal short-circuiting and localized thermal runaway. Conventional liquid-state electrolytes, being inherently flammable organic systems, exacerbate these risks and fundamentally constrain LMB implementation. SSEs, by contrast, circumvent these limitations through intrinsic inflammable properties and mechanical robustness.[6–9]

However, in contrast to liquid electrolyte systems that enable conformal interfacial contact with the LMA, the inherent rigidity of SSEs results in poor solid–solid interfacial adhesion. This inadequate physical contact at the LMA/SSE interface generates substantial interfacial resistance and inhomogeneous Li^+ flux, which collectively deteriorate the electrochemical performance of ASSLBs.[10] The fundamental electrochemical reaction governing lithium deposition/dissolution can be expressed as: $Li \leftrightarrow Li^+ + e^-$. This reversible

[a]State Key Laboratory of Precision and Intelligent Chemistry, School of Chemistry and Materials Science, University of Science and Technology of China, Hefei, 230026, China. E-mail: zhoujb01@ustc.edu.cn, jiaosh@ustc.edu.cn
[b]School of Chemistry and Chemical Engineering, Shandong University of Technology, Zibo, 255000, China
[c]Hefei National Research Center for Physical Science at Microscale, School of Chemistry and Materials Science, University of Science and Technology of China, Hefei, 230026, China
[d]Guangdong Provincial Key Laboratory of Nano-Micro Materials Research, Peking University Shenzhen Graduate School, Shenzhen, Guangdong 518000, China

redox process inevitably induces substantial volumetric fluctuations within the cells. The relationship between the areal capacity (Q_A, in mAh cm^{-2}) of an LMA and the resulting thickness variation (Δd_{Li}) can be derived through the following quantitative expression:

$$\Delta d_{Li} = \frac{m_{Li}}{\rho_{Li} \cdot A} = \frac{n_{Li} \cdot M_{Li}}{\rho_{Li} \cdot A} = \frac{Q_A \cdot M_{Li}}{Z_c \cdot F \cdot \rho_{Li}}$$

where M_{Li} and ρ_{Li} represent the molar mass and density of lithium metal, respectively. Z_c denotes the number of electrons transferred (Z_c = 1 for Li^+) and F is Faraday's constant. Taking a 30-layer ASSLB with a stacked configuration (nominal capacity: 2 Ah, electrode dimensions: 4 cm × 5 cm) as a representative case, the system necessitates a Q_A exceeding 3.3 mAh cm^{-2} to meet practical energy density requirements.[11,12] Therefore, each cycle of lithium deposition and stripping induces a substantial thickness variation exceeding 16 μm per electrode side, accumulating into an overall dimensional change of around 480 μm. It should be emphasized that these calculations are based on the assumption of perfectly dense lithium deposition and stripping behaviors. In practical scenarios, the actual volume fluctuations are more pronounced due to the inevitable formation of porous lithium structures under diverse charge/discharge conditions. Particularly when operating beyond the critical current density (CCD), this phenomenon becomes exacerbated through the generation of detrimental voids within the electrode structures.[13] The inhomogeneous Li deposition behavior in solid-state systems generates localized current hotspots that accelerate dendrite formation and electrolyte fracture. These effects, combined with significant volume changes and interfacial void generation, continue to impede the practical adoption of LMAs in solid-state batteries (SSBs).

To address these challenges, three strategic approaches have emerged, such as interfacial engineering to stabilize electrode–electrolyte interfaces, rational design of SSEs with enhanced ionic conductivity, and construction of composite electrodes to accommodate volume fluctuations.[14–16] Foremost among these strategies, constructing 3D LMAs represents the most comprehensive approach for simultaneously addressing these challenges.[17–19] Notably, the high specific surface area of 3D hosts enables the dispersion of applied current density, thereby reducing the local current density at the anode and facilitating uniform lithium deposition. Concurrently, the interpenetrating architecture compartmentalizes bulk lithium into discrete domains, effectively accommodating volume fluctuations during cycling and minimizing internal stress accumulation. 3D LMAs are typically engineered from carbon-based matrices, metal-based frameworks, or other lithiophilic compounds. These materials synergistically (i) lower nucleation energy barriers to promote homogeneous deposition, and (ii) direct deposition to mitigate side reactions with SSEs. While 3D LMA strategies have been extensively reviewed for liquid-electrolyte systems, their application in solid-state batteries remains largely unexplored. Given the critical role of 3D architectures in enabling high-performance ASSLBs, a systematic examination of recent advances is imperative.

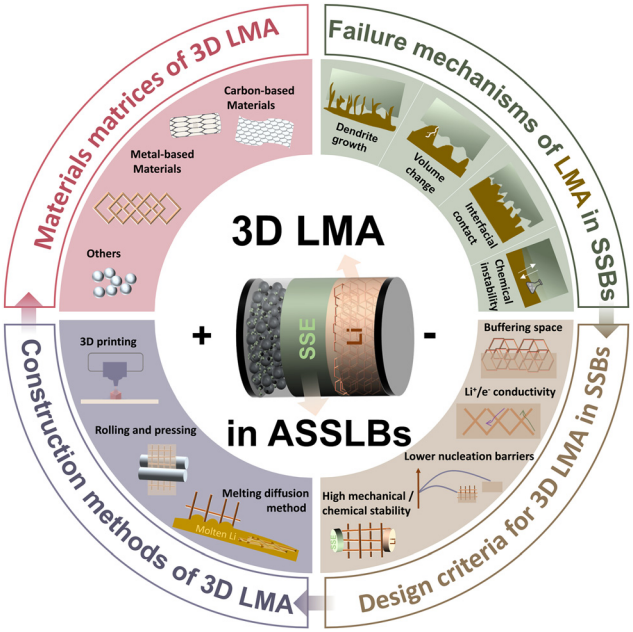

Fig. 1 Schematic illustration of challenges and mitigation strategies for 3D LMA in ASSLBs.

Herein, this review comprehensively examines recent advances in 3D LMAs for SSBs, structured around four pivotal dimensions (Fig. 1). First, we elucidate the failure mechanisms inherent to conventional ASSLBs, specifically addressing dendritic lithium propagation, interfacial contact loss, mechanical instabilities induced by volumetric fluctuations, and chemical degradation phenomena at LMA–SSE interfaces. To overcome these challenges, we establish fundamental design principles for 3D LMA architectures, emphasizing synergistic structural engineering and host material optimization. Next, contemporary fabrication methodologies including melt infiltration, mechanical compression, and additive manufacturing are critically evaluated regarding their technical viability and limitations. We then categorize and analyze 3D LMA material matrices as carbon-based frameworks, metallic scaffolds, and alternative systems. Finally, persistent challenges and future research trajectories for deploying 3D architectures in ASSLBs are systematically outlined. This review aims to catalyze further innovation in developing high-performance ASSLBs.

2. Failure mechanisms of LMA in SSBs

With the implementation of SSEs, the failure mechanisms of LMAs originate primarily from three critical factors: dendritic lithium propagation, mechanical instability induced by volumetric fluctuations/interfacial contact loss, and chemical degradation at the LMA/SSE interface. These phenomena are

intrinsically governed by the nucleation–deposition–stripping dynamics of metallic lithium.

2.1 Dendrite growth

The dendrite initiation and propagation of lithium are complex and governed by fundamental electrochemical principles. Classical nucleation theory posits that lithium nucleation initiates when the cell potential reaches a critical threshold, commonly referred to as the nucleation overpotential (Fig. 2a). This overpotential serves as a quantitative indicator of the heterogeneous nucleation behaviors exhibited by lithium across different substrate materials.[20,26] The judicious selection of host materials capable of modulating lithium nucleation behavior represents a crucial determinant for achieving subsequent uniform lithium deposition. During the electro-deposition processes, the resultant lithium morphology is simultaneously influenced by two key parameters: the deposition overpotential and the applied current density. Regarding these two factors, Pei *et al.* proposed that increasing the deposition overpotential can reduce the size of crystal nuclei, and lower current densities can lead to more densely packed lithium nucleation.[27] However, this presents fundamental trade-offs that higher deposition overpotentials signify higher kinetic barriers for lithium deposition on the substrate and practical battery operation necessitates high current density conditions to meet power density requirements, exacerbating the challenge of maintaining uniform deposition. The manifestation of non-uniform lithium deposition, commonly termed lithium dendrite formation, constitutes a significant technological barrier for lithium metal batteries, particularly under high-current operation conditions. This phenomenon not only compromises the electrochemical performance, but also raises critical safety concerns.

Among prevailing theoretical frameworks for lithium dendrite formation, the space–charge model has gained broad acceptance (Fig. 2b and c).[21] This theory posits that dendritic propagation originates from ionic mobility disparities between anions and cations, inducing space–charge accumulation at the anode–electrolyte interface and triggering interfacial instability. With the implementation of SSEs, inherently low ionic conductivity and poor interfacial contact may exacerbate this space–charge effect. During lithium deposition, rapid cation consumption drives Li^+ concentration at the anode surface toward depletion, establishing a high-intensity electric field that accelerates non-uniform Li^+ deposition and initiates dendrite growth. The critical onset time for dendrite initiation is defined as Sand's time (Fig. 2d),[22,28] mathematically expressed by the following equation:

$$t_{\text{sand}} = \frac{\pi D(Z_c F C_0)^2}{4J^2 {\tau_a}^2}$$

Here, Z_c denotes the charge number of the cation (Z_c = 1, Li^+), D is the ambipolar diffusion coefficient, C_0 is the initial cation concentration, J is the current density, and τ_a is the anion transference number. This equation reveals that dendritic lithium propagation preferentially occurs under high

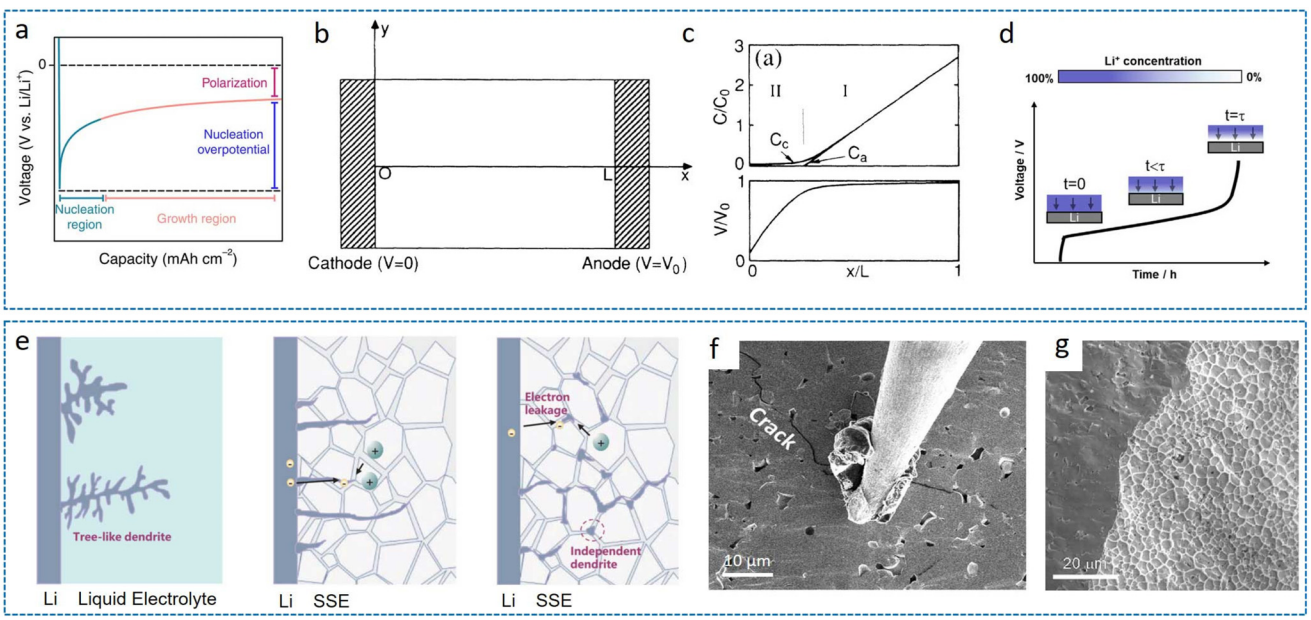

Fig. 2 Fundamental mechanisms governing lithium deposition behavior. (a) Typical voltage profile of the Li deposition process.[20] Reproduced with permission from IOP Publishing, copyright 2022. (b) Schematic cell configuration and (c) profile of the ion concentrations (C_a, C_c) and electrostatic potential (V) distribution under idealized uniform deposition conditions.[21] Reproduced with permission from American Physical Society, copyright 1990. (d) Schematic illustration of Sand's time.[22] (e) Comparative dendrite propagation mechanisms in liquid electrolyte *versus* SSEs.[23] Reproduced with permission from John Wiley & Sons, copyright 2023. (f) SEM evidence of SSE fracture initiated by dendritic lithium penetration.[24] (g) Preferential lithium propagation through grain boundaries in polycrystalline SSEs.[25] Reproduced with permission from Elsevier, copyright 2017.

current density (J) and low ionic diffusion coefficient (D) conditions. For the former, the CCD serves as a widely adopted metric to evaluate interfacial tolerance to current loads. 3D porous architectures engineered with a high surface area effectively reduce the local current density, thereby suppressing dendrite nucleation through electrochemical kinetic control. For the latter, SSEs establish intrinsic physical barriers *via* enhanced mechanical rigidity, fundamentally inhibiting vertical dendrite penetration. These dual mechanisms on electrochemical kinetic regulation and physical obstruction synergistically enhance the interfacial stability in ASSLBs.

However, dendrite penetration through SSEs, leading to internal short circuits, remains prevalent in practical applications. In liquid electrolytes, the morphology of lithium deposits can be needle-like or moss-like.[29] Despite the theoretical prediction that SSEs' elevated shear modulus should mechanically suppress dendrite proliferation, experimental evidence confirms persistent lithium dendrite penetration through SSEs, culminating in internal short circuits, as illustrated in Fig. 2e.[23,30] Advanced characterization techniques now enable unprecedented visualization of dendrite dynamics. Kolmakov *et al.* utilized *in situ* SEM-Auger spectroscopy to demonstrate current-density-dependent dendrite evolution modulated by trace O_2.[31] Shearing *et al.* achieved nanoscale 3D reconstruction of lithium protrusions in short-circuited SSEs *via* X-ray computed tomography (XCT).[32] Progress in characterization technology has deepened the understanding of dendrite formation. Taking inorganic SSEs as an example, these studies reveal two distinct failure modes: interface-induced fracture and internal lithium nucleation.[33] These correspond to the anode-initiated mechanism (Fig. 2f) and grain boundary (GB)-initiated mechanism (Fig. 2g) of lithium dendrite formation, respectively. The mechanism of lithium deposition within bulk SSEs was first elucidated by Wang *et al.* through comparative analysis of the representative systems of LiPON, $Li_7La_3Zr_2O_{12}$ (LLZO), and amorphous Li_3PS_4 during dendrite formation.[34] *Operando* characterization revealed that Li accumulation occurs directly within bulk LLZO and Li_3PS_4 due to their high electronic conductivity, thereby forming dendrites. Consequently, suppressing the electronic conductivity, rather than further enhancing the ionic conductivity of SSEs, is paramount for the success of ASSLBs. Computational studies by Ma *et al.* combining AIMD with theoretical modeling identified interfacial instability, rather than GB reduction, as the primary driver in Li_6PS_5Cl (LPSC) systems.[23] Their work demonstrates significantly higher energy barriers for GB-initiated nucleation compared to anode-surface initiation, positioning interfacial engineering as a critical focus for dendrite suppression. Moreover, Kim *et al.* recently identified through comprehensive techniques, including laser-induced breakdown spectroscopy, that microscopic dendrite penetration generates voltage fluctuations that dissolve transition metals (TMs) from cathodes with the electrolyte of PEO-LLZO. These dissolved TMs migrate to the anode, functioning as preferential nucleation sites that accelerate dendrite growth, as a process termed voltage noise failure (VNF).[35] This mechanism extends beyond traditional current-density/mechanical-stress paradigms, suggesting cathode modification as a viable strategy for enhancing the cycling stability of SSBs.

2.2 Mechanical instability

In ASSLBs, the absence of buffer space between LMAs and SSEs confines lithium deposition within constrained volumes. Consequently, significant electrode volume changes during cycling generate substantial interfacial stresses, compressing the SSE and inducing mechanical instability at interfaces. This stress accumulation promotes LMA fatigue, electrolyte penetration and dendrite-induced short circuits. During stripping, the plastically deformed SSE fails to recover elastically, creating interfacial voids that degrade contact integrity and increase interfacial impedance. Huang *et al.* determined that the failure of ASSLBs is closely linked to the fatigue of the LMA during cycling by the *operando* scanning electron microscopy (SEM) test and phase-field simulations.[36] The fatigue behavior adheres to the Coffin–Manson equation in mechanics, confirming it as a universal phenomenon in SSBs. Xin *et al.* employed *in situ* electron microscopy to elucidate the nanoscale transition from soft-short to hard-short circuits in various kinds of inorganic SSEs induced by electron leakage, while highlighting the stress-buffering role of the composite inorganic/polymer SSE design.[37]

2.2.1 Volume change. Beyond dendrite formation, the substantial volumetric deformation during Li plating/stripping, as detailed above, induces electrode mechanical instability. The mechanical inability to accommodate these volume fluctuations ultimately triggers cell failure. Shearing *et al.* tracked the 3D morphological evolution of Li_3PS_4 until short-circuit *via in situ* synchrotron XCT.[40] Cracks alternately initiate from both electrode/electrolyte interfaces during degradation, with accelerated electrolyte deterioration in the initial cycles. This highlights the critical role of strain energy release during early cycling in accelerating mechanical failure. Yang *et al.* employed zero-strain $Li_4Ti_5O_{12}$ (LTO) as the counter electrode, performing *in situ* stress quantification in LTO/SSE/Li cells and elucidating electrochemomechanical coupling through finite-element simulations (Fig. 3a).[38] Their results reveal cell failure after 4 cycles at a capacity of 1.5 mAh (Fig. 3b), where Li deposition rates exceed its creep (the viscoplastic deformation rate under stress/temperature) rate, causing stress accumulation and global mechanical destabilization. A "safe zone" for stable operation was identified, requiring current densities below the CCD and limited capacities (minimized internal stress).

2.2.2 Solid–solid interface contact. Poor interfacial contact poses a fundamental challenge in ASSLBs, where lattice mismatch and cyclic plating/stripping generate interfacial voids. While interfacial instability prompts creep deformation in lithium metal as a mechanism for stress relief and void filling, extensive voiding causes a critical loss of physical contact and cell failure. Furthermore, incomplete contact triggers a cascade of detrimental effects: it localizes the current flow (Fig. 3c), disturbs the uniform Li^+ flux, alters the creep response, and ultimately facilitates dendrite formation and

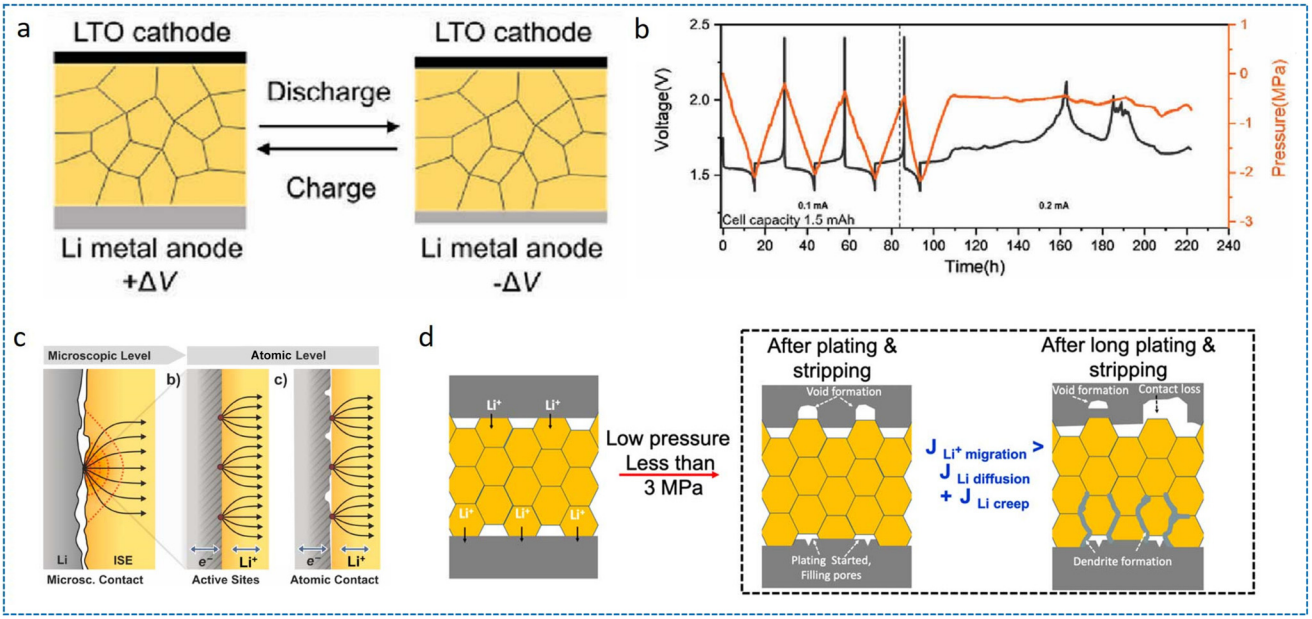

Fig. 3 (a) Schematic of Li^+ flux-driven volumetric changes in LTO/SSE/Li cell configurations and (b) galvanostatic cycling profiles with synchronized stack pressure evolution with a capacity of 1.5 mAh.[38] Reproduced with permission from John Wiley & Sons, copyright 2023. (c) Current constriction phenomena under inhomogeneous electrode–electrolyte contact.[33] Reproduced with permission from American Chemical Society, copyright 2020. (d) Schematic of Li plating/stripping under low stack pressure (<3 MPa) where significant void formation occurs on the stripping side (top panel) and Li deposition on the plating side (bottom panel) fills the pores.[39] Reproduced with permission from American Chemical Society, copyright 2020.

structural degradation. Lin *et al.* investigated that the nucleation and growth of interfacial voids are strongly correlated with the stripping current density.[41] Lower stripping currents promote the concurrent growth of 2D and 3D voids, generating fewer but deeper cavities. In contrast, higher currents predominantly drive 2D void growth, producing numerous shallow voids and thinner void layers. Furthermore, the study demonstrates that the Li–Mg alloy structure effectively suppresses interfacial void formation, revealing that elevated Mg concentrations impede Li^+ transport within the electrode. These findings underscore the importance of balancing the interfacial stability with ionic diffusion capacity in the optimization of LMA. Bruce *et al.* quantified the CCD for Li/LPSC/Li cells at 0.2 and 1.0 mA cm^{-2} under 3 and 7 MPa, respectively.[42] The pressure-dependent CCD confirms creep-dominated lithium transport over bulk diffusion. Meng *et al.* further revealed that excessive pressure (75 MPa) induces Li creep deformation, causing mechanical short-circuit before electrochemical cycling.[39] Conversely, under insufficient operation pressure (3 MPa), inhomogeneous stripping creates interfacial voids that degrade contact and elevate impedance until failure (Fig. 3d). Zhu *et al.* employed *in situ* neutron imaging and XCT to demonstrate that external pressure actively mitigates dendrite propagation by enhancing Li creep during "soft-short" events.[43] Complementarily, Bruce *et al.* proposed a dendrite failure mechanism *via operando* XCT-spatially mapped XRD, establishing that dendrite propagation exhibits pressure-sensitive kinetics that reducing the stack pressure significantly suppresses dendrite advancement even after initiation, thereby delaying short-circuit.[44] This reveals a critical trade-off that adequate pressure maintains interfacial integrity during stripping, yet simultaneously drives dendrite propagation during plating. Consequently, optimizing the mechanical structural performance by means of balancing the interfacial stability against dendrite driving forces is essential.[45] Beyond pressure modulation, interfacial engineering provides alternative solutions. For example, Fan *et al.* addressed this by integrating polymer-electrolyte-coated garnet SSEs with 3D-structured Li anodes, achieving conformal solid–solid contact without excessive stack pressure.[46]

2.3 Chemical instability

A fundamental prerequisite for the stable operation of ASSLBs is the thermodynamic stability of the SSE at the LMA/SSE interface. However, the low electrochemical potential of Li/Li^+ inevitably drives reduction reactions when the lowest unoccupied molecular orbital (LUMO) energy level of the SSE lies above the Fermi level of metallic Li. This energy misalignment triggers complex interfacial reduction, thereby nucleating localized current hotspots that propagate dendrite growth and induce catastrophic failure.[47] Such interfacial side reactions are particularly prevalent in sulfide-based SSEs, such as LPSC, Li_3PS_4 (LPS), and $Li_{10}GeP_2S_{12}$ (LGPS). The resulting interphase, typically comprising Li_2S, Li_3P, and LiCl, often exhibits high ionic conductivity and favorable interfacial energy, which can promote uniform lithium deposition while suppressing dendrite growth and persistent side reactions.[48] However, a significant risk arises if the interphase contains electronically con-

ductive byproducts, such as Li_2S_2 and $Li_{15}Ge_4$. Watanabe *et al.* employed *operando* XCT to track the 3D morphological evolution of LPS in contact with lithium metal, revealing that such electron conductive reaction products can induce lithium deposition within the electrolyte bulk, ultimately resulting in battery failure.[49] To mitigate these issues, primary strategies have focused on two key approaches of designing electron-insulating electrolytes and introducing functional interfacial buffer layers. Sun *et al.* reported a vacancy-rich-β-Li_3N SSE that combines high ionic conductivity with exceptional lithium compatibility and air stability, providing a critical breakthrough for enhancing the performance of ASSLBs.[50] The symmetric cells employing vacancy-rich β-Li_3N as the SSE achieved an ultrahigh CCD of 45 mA cm^{-2} and stable lithium stripping/plating for over 2000 cycles, demonstrating the high chemical stability and superior compatibility of the β-Li_3N layer with Li metal. Ci *et al.* exploited the self-limiting reaction between lithium and LPSC to *in situ* fabricate a hybrid interphase layer (denoted as LPSC@Li) on the LMA surface, which effectively isolates the LMA from direct contact with the SSE membrane, thereby mitigating side reactions and suppressing the formation of lithium dendrites.[51] Thus, the assembled LPSC@Li/LPSC/$LiNi_{0.8}Co_{0.1}Mn_{0.1}O_2$ (NCM811) full cell delivered remarkable cycling stability, maintaining 76.3% capacity retention over 800 cycles at a 2.0C rate.

3. Design criteria for 3D LMA in SSBs

To overcome the challenges in ASSLBs, 3D LMAs fabricated either by infusing Li into porous scaffolds or through specialized structural engineering represent an effective strategy.[52–54] These architectures feature interconnected ion/electron transport networks and enhanced mechanical resilience. Crucially, surface modification with lithiophilic materials (materials with high thermodynamic affinity for lithium, such as Ag, Mg, and ZnO) is typically employed to mitigate interfacial energy barriers and optimize lithium deposition kinetics. As illustrated in Fig. 4a, optimal 3D LMA design necessitates: (i) ample porous volume accommodating Li^+ flux redistribution and volume fluctuations, (ii) bicontinuous ion/electron transport pathways ensuring homogeneous current distribution, (iii) reduced nucleation overpotential enabling spatially uniform Li deposition, (iv) mechanically robust frameworks resisting deformation during plating/stripping, and (v) thermodynamic stability against metallic Li to prevent parasitic interfacial reactions.

3.1 Structural design

The structural design of LMAs can be classified by structural typologies, such as porous scaffolds, gradient architectures, and low tortuosity frameworks. Firstly, porous scaffolds leverage their high specific surface area and interconnected pore channels to reduce the localized current density and accommodate volume changes during cycling. However, a key limitation is the persistence of microscale interfacial voids when these scaffolds are directly assembled with SSEs. To address this, recent approaches employ *in situ* reactions like electrolyte polymerization or interfacial alloying to improve solid–solid contact.[57] Guo *et al.* designed an integrated cell architecture where a Li/carbon fiber (Li/CF) 3D anode connects to the cathode *via* a self-polymerized gel electrolyte (Fig. 4b and c).[55] This gel confines the liquid electrolyte within the CF matrix, mitigating solid–solid contact loss while the *in situ*-formed polymer electrolyte with a Young's modulus of ~13.3 GPa simultaneously suppresses dendrite penetration and ensures safety. Secondly, gradient design represents a strategic methodology that spatially modulates progressive variations in material composition, microstructure, or functionality across

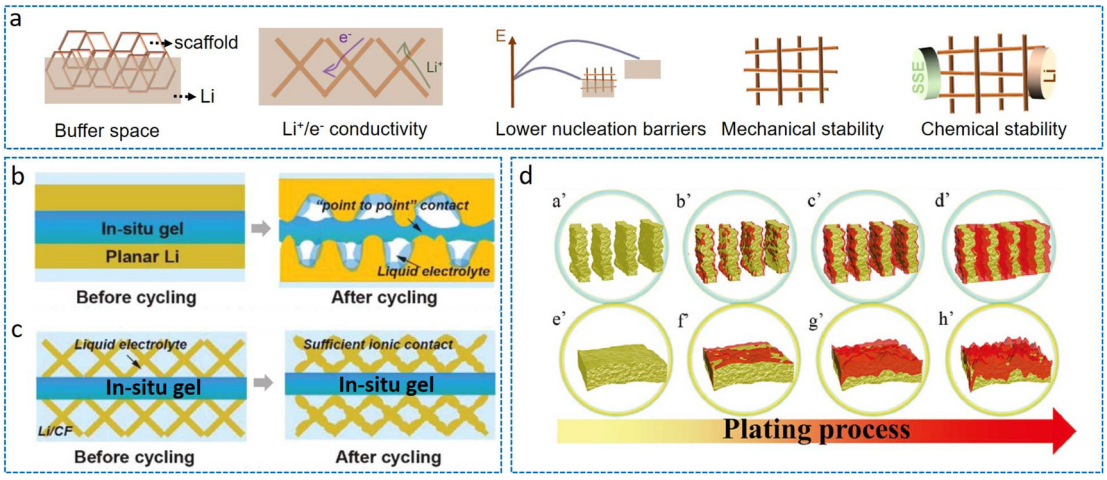

Fig. 4 (a) Design principles for 3D LMAs in SSBs. Schematic comparison of (b) inhomogeneous deposition/dissolution on planar Li *versus* (c) confined electro-deposition within Li/CF, mitigating void formation and stress accumulation.[55] Reproduced with permission from John Wiley & Sons, copyright 2019. (d) Confined Li plating within VA-Li microchannels (a′–d′) with suppressing vertical dendrite propagation and (e′–h′) uncontrolled dendritic growth on bare Li under identical conditions.[56] Reproduced with permission from John Wiley & Sons, copyright 2020.

electrode architectures, thereby synergistically addressing multiscale interfacial challenges. While such gradient designs for 3D lithium anodes have seen relatively broad application in liquid-electrolyte batteries, their implementation in ASSLBs remains comparatively limited. Yu *et al.* infiltrated molten lithium into g-C_3N_4 coated carbon cloth (CC@g-C_3N_4), forming a 3D LMA featuring an *in situ* formed gradient Li_3N interface.[58] The high ionic conductivity and electrochemical stability of Li_3N accelerate Li^+ diffusion across the anode/electrolyte interface while suppressing parasitic reactions, enabling uniform Li^+ flux and reducing the interfacial resistance. Thirdly, tortuosity serves as a pivotal topological parameter that governs the spatial distribution of the Li^+ flux during cycling, thus fundamentally influencing lithium deposition behavior. Defined as the degree of twisting and complexity of ion transport pathways within a porous medium, higher tortuosity corresponds to more convoluted diffusion trajectories and increased transport resistance. In practical 3D LMAs, highly tortuous frameworks impede efficient Li^+ diffusion, promoting preferential lithium deposition near the LMA–SSE interface. In contrast, vertically aligned architectures with low tortuosity facilitate rapid and homogeneous Li^+ transport, mitigating the accumulation of inactive lithium at the interface. Therefore, emphasizing low-tortuosity structural designs is critical in the development of advanced 3D LMA. Sun *et al.* engineered a vertically aligned Li (VA-Li) anode *via* 3D printing.[56] The CNT@ZnO lithiophilic microwalls enable laterally confined deposition, redirecting Li growth parallel to the electrode surface and preventing dendritic penetration through the electrolyte (Fig. 4d). Concurrently, the low tortuosity structure accelerates Li^+ transport and protects the electrolyte. Consequently, VA-Li symmetric cells achieve 300 h cycling at 3 mA cm^{-2}/3 mAh cm^{-2}, illustrating the unique advantages of this structure in designing 3D LMA.

3.2 Material design

An optimal 3D LMA necessitates both structural integrity and substrate stability, where the scaffold's lithiophilicity and electronic conductivity critically govern lithium deposition sites. Lithiophilic materials guide the preferential nucleation of Li^+, promoting ion transport and thereby suppressing dendrite formation. In contrast, lithiophobic materials do not directly promote lithium deposition; instead, they induce lithium to grow uniformly beneath the interface or through interlayer channels and suppress interfacial side reactions due to their inherent stability. Notably, the electrical conductivity of the host scaffold plays a decisive role in determining the location of lithium deposition (Fig. 5a). In highly conductive scaffolds, Li^+ can be immediately reduced to metallic lithium upon contact, resulting in deposition predominantly in the upper region (adjacent to the electrolyte) of the host. Conversely, in scaffolds with low conductivity, Li^+ permeates rapidly through the structure and reaches the bottom region (near the current collector) before being reduced. When Li preferentially accumulates on the upper region, the thickening Li layer obstructs lower Li^+ transport channels and induces void formation, thereby undermining the 3D architecture's utilization efficiency. Therefore, the "bottom-up" lithium deposition behavior is considered an important innovative strategy for achieving more stable battery performance. Wang *et al.* employed *in situ* electron microscopy to resolve Li plating/stripping dynamics, designing a mixed ionic-electronic conducting (MIEC) host with Ag-decorated carbon spheres.[60] This structure enables long-range Li diffusion (~100 μm), facilitating deposition/dissolution distal from interfaces and suppressing dendrites/voids *via* "bottom-up" Li deposition.[61,62] Similarly, Peng *et al.* engineered a conductivity/overpotential-graded 3D Si@carbon nanofiber (CNFs)@ZnO–ZnO–Cu skeleton (SCZ) scaffold that guides homogeneous upward Li growth, achiev-

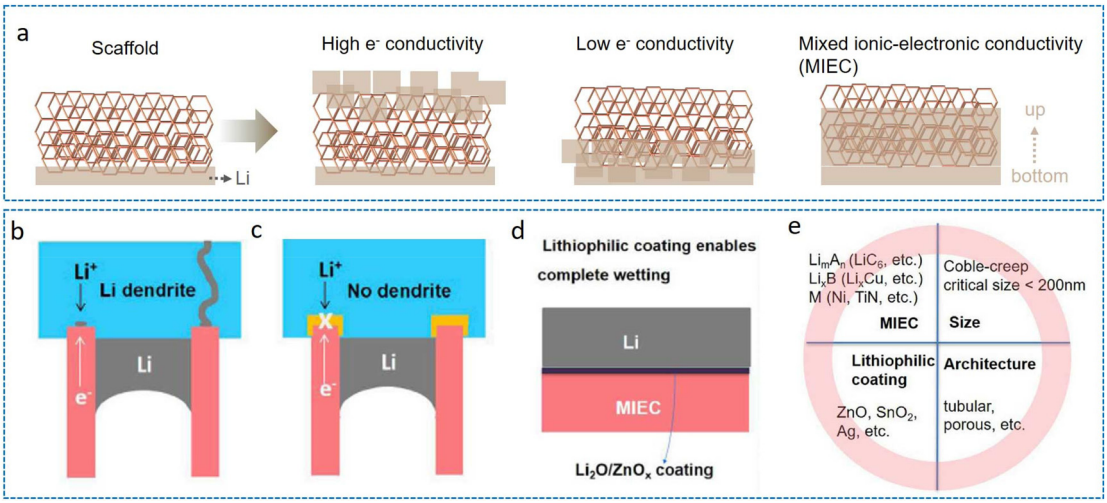

Fig. 5 (a) Schematic illustration of the influence of scaffold materials on lithium deposition behavior. (b and c) Working mechanisms of MIEC (b) without or with (c) ELI in 3D LMA. (d) The great wetting performances with the existence of a lithiophilic coating. (e) The design details with respect to the 3D porous MIEC/ELI structures.[59] Reproduced with permission from Elsevier, copyright 2020.

ing 2000 cycles at 5C for SCZ-Li‖$LiFePO_4$ full cells.[63] Further advancing this paradigm, Li *et al.* demonstrated that 3D porous MIEC/electronic and Li^+ insulator (ELI) structure composite metallic Li can realize a stable deposition and stripping process through viscous creep behavior (Fig. 5b–d).[59] The observed Li creeping behavior corresponds to a viscoplastic flow phenomenon, wherein lithium crystals exhibit liquid-like deformation through grain boundary sliding during plating/stripping cycles, which is a process governed by Herring's solid diffusion viscosity model that dominates mass transport at microscale interfaces. To optimize interfacial dynamics, lithiophilic coatings (*e.g.*, ZnO, Li_2O) are engineered on MIEC phases (LiC_6, Li_9Al_4, $Li_{22}Si_5$) to enhance Li wettability and reduce nucleation barriers. Conversely, at MIEC termini where Li convergence induces localized stress concentrations, lithiophobic ELI barriers (*e.g.*, BeO, SrF_2) create inert mechanical interlocking with SSEs (Fig. 5e), thereby suppressing dendritic protrusion by redirecting the Li^+ flux toward defect-free regions. This synergistic MIEC/ELI architecture establishes a fundamental design paradigm for 3D LMAs, providing theoretical guidance for achieving spatially controlled Li deposition.

Notably, in the electrode assembly paradigm for ASSLBs, SSEs inherently function as multifunctional scaffolds.[64,65] Hu *et al.* engineered a bilayer garnet SSE with a porous/dense architecture, wherein the porous layer serves as a volume-buffering Li host with enhanced interfacial contact, while the dense layer acts as a dendrite-blocking separator.[66] Similarly, Liu *et al.* developed a corrugated 3D nanowire-bulk ceramic-nanowire (NCN) skeleton *via* the sol–gel method and electrospinning method, where the ceramic network encapsulated by the PEO-based electrolyte provides both Li deposition buffering space and ion-transport pathways, mitigating stress accumulation during cycling.[67] To further amplify ion transport kinetics, Zeng *et al.* fabricated a sub-50 μm polyethylene glycol diacrylate (PEGDA) electrolyte with vertically aligned ion-conducting networks (>100 μm) *via* 3D printing, whose ultra-low tortuosity and enlarged interfacial area simultaneously homogenize Li deposition and accelerate Li^+ flux.[68] Traditionally, the inherent insulating nature of solid electrolytes has severely limited their application in electrode integration, making precise modulation of the electrode–electrolyte interfacial region a critical strategy for developing high-performance single-phase electrolyte systems, and advanced interfacial engineering strategies offer solutions. Wachsman *et al.* achieved a record CCD of 100 mA cm^{-2} through multivalent cation doping in garnet SSEs, constructing a MIEC–electrolyte–MIEC sandwich architecture that redistributes interfacial electric fields.[69] Complementarily, unique 3D architectures can also be derived from *in situ* reactions of electrolytes. Li *et al.* leveraged *in situ* reactions by depositing perovskite $LaRuO_3$ on $Li_{6.4}La_3Zr_{1.4}Ta_{0.6}O_{12}$ (LLZTO), inducing the formation of $Li_2Zr_2O_7$ scaffolds that eliminate interfacial voids and guide spatially ordered Li deposition.[70]

4. Construction methods of 3D LMA

The fabrication methodologies for 3D LMAs integrated with SSEs, including molten Li infusion, mechanical compression, and 3D printing, share fundamental parallels with those employed in liquid-electrolyte systems. Each technique exhibits distinct advantages and constraints. Molten infusion enables conformal Li filling but requires precise thermal control to suppress interfacial reactions, mechanical compression enhances electrode–electrolyte contact yet risks microcrack propagation under excessive pressure, while 3D printing achieves programmable architectures but faces resolution limits for submicron features. Consequently, optimal selection must reconcile targeted pore geometry, lithiophilic modification requirements, and interfacial stability criteria, as governed by the processing-structure–property relationship. To provide a more intuitive description, Table 1 summarizes the composition and corresponding electrochemical performance of different 3D lithium hosts.

4.1 Melting diffusion method

By leveraging metallic lithium's low melting point (180 °C), researchers fabricate composite LMAs by infiltrating molten Li into 3D porous current collectors. Wang *et al.* pioneered this approach by pressing an Ag-coated Cu mesh (ACM) onto the LLZTO electrolyte, followed by thermal infusion of molten Li to form an integrated electrode–electrolyte assembly (Fig. 6a).[71] The Ag lithiophilic coating enhances interfacial wetting while the 3D framework directs uniform Li deposition. Building on this principle, capillary-driven infiltration strategies have been advanced. Fan *et al.* demonstrated molten Li climbing through Ni foam *via* capillary action,[77] while Guo *et al.* engineered a Li/CF composite by exploiting capillary forces between molten Li and CF scaffolds (Fig. 6b).[55] To mitigate interfacial stress, Guo *et al.* further introduced a solid polymer electrolyte (SPE) interlayer, enabling symmetric cells to achieve >700 cycles at 0.2 mA cm^{-2}. Hu *et al.* extended this paradigm by co-sintering tape-cast porous/dense bilayer $Li_7La_{2.75}Ca_{0.25}Zr_{1.75}Nb_{0.25}O_{12}$ (LLCZN) garnet electrolytes, where the porous layer accommodates molten Li to form a volume-stable 3D host, while the dense layer blocks dendrite penetration.[78] This architecture supported reversible cycling of $Li(Ni_{0.5}Mn_{0.3}Co_{0.2})O_2$ (NCM523) cathodes at 32 mg cm^{-2} areal loading. Subsequently, they developed an "all-in-one" Li–S battery using a porous–dense–porous trilayer SSE.[79] Despite the operational simplicity, the melting diffusion method faces critical constraints that scaffolds must exhibit high lithiophilicity to overcome Li surface tension, while high-temperature processing risks triggering Li extrusion through subsurface pores, exacerbating interfacial degradation, and rapid thermal cycling further induces stress concentration at grain boundaries, limiting scalability.

Table 1 Electrochemical performance of different 3D LMA in previously reported SSBs

Materials	Configuration	Symmetric cell (cycle, current density [mA cm^{-2}], capacity [mAh cm^{-2}])	CCD [mA cm^{-2}], capacity [mAh cm^{-2}]	Symmetric cell with planar LMA	Cathode (loading [mg cm^{-2}], working temperature)	Full cell (cycles, current density [mA g^{-1}], capacity [mAh g^{-1}] (stack pressure))	Full cell with planar LMA	Electrolyte	Ref.
Carbon-based materials	3D Li/CF	560 h, 0.5, 0.5	—	280 h, 0.5, 0.5	$LiFePO_4$ (LFP) (3.5–4.0, —)	120, 0.2C, 129 (—)	52, 0.2C, 68	TTE gel	55
	3D-MCF (SSE@ ZnO@CNTs)	180 h, 1.0, 1.0 140 h, 3.0, 3.0	—	—	Polysulfide (—, —)	50, 1.0, 3.0 mAh cm^{-2} (—)	—	LLZO	61
	$Li_{3.75}Si$-CNT (MIEC)	35 cycles, —, 3.0	—	—	NCM811 (20, 60 °C)	200, 0.98, ~2.3 mAh cm^{-2} (5 MPa)	60, 0.35C, ~0.5 mAh cm^{-2}	LPSC	62
	CVD-treated YP-50F	—	—	—	$LiNi_{0.9}Co_{0.05}Mn_{0.05}O_2$ (4.1 mAh cm^{-2}, 60 °C)	50, 0.2 mA cm^{-2} (charge) &0.1 mA cm^{-2} (discharge), 80 (—)	—	LPSC	82
	Li_3PS_4-graphite	40 cycles, —, 0.75 (Li-3D cell)	1.4, 1.4	8 cycles, —, 0.75 (Li–Cu cell)	$LiNi_{0.85}Co_{0.10}Al_{0.05}O_2$ (NCA) (0.75 mAh cm^{-2}, 35 °C)	80, 0.1 mA cm^{-2}, ~60 (NCA-3D) (90 MPa)	30, 0.1 mA cm^{-2}, ~20 (NCA-Cu)	LPS	83
	Li_7N_2I-CNT and Li_7N_2I-Mg	~650 h, 4.0, 4.0	4.0, 4.0	— (CCD: 0.2, 0.2)	NCM811 (2.2 mAh cm^{-2}, 60 °C)	350, 1.1 mA cm^{-2}, ~140 (~1 MPa)	—	LNI	84
	CC/Li/Li_3N (carbon cloth@g-C_3N_4)	1000 h, 2.0, 2.0	—	—	LFP (2, —)	100, 0.1C, 140 (—)	—	LLZO	58
	LM_5G_{50}	1500 h, 0.3, 0.3	1.3, 1.3	221 h, 0.3, 0.3	NCM622 (7, 25 °C)	300, 0.1C, ~70 (—)	46, 0.1C, short-circuit	LPSC	86
Metal-based materials	Ni_C_Ag	100 cycles, 2.0, 0.5 (Li-3D cell)	—	6 cycles, 2.0, 0.5 (Li–Ni cell)	NCM811 (17, 30 °C)	100, 0.68 mA cm^{-2}, 1.22 mAh cm^{-2} (NCM811-3D) (~30 MPa)	8, 0.68 mA cm^{-2}, short-circuit (NCM811-Ni)	LPS/$Li_6PS_5Cl_{0.5}Br_{0.5}$ (LPSClBr)	53
	VA-Li (CNT@ZnO)	650 h, 0.5, 0.5 300 h, 3.0, 3.0	>3	~100 h, 0.5, 0.5	LFP (2.66, 60 °C)	800, 2C, 112.5/2000, 4C, 89.4 (30 MPa)	60, 2C, short-circuit	Poly(ethylene glycol) dimethyl ether (PEGDME)	56
	Ag@Cu mesh (ACM)	800 h, 0.1, —	0.3, —	20 h, 0.1, —	LFP (—, 25 °C)	300, 0.5C, 119 (—)	—	LLZTO	71
	LiSnC	400 h, 0.5, 0.2	1.2, 1.2	148 h, 0.5, 0.2	$LiNi_{0.9}Co_{0.05}Mn_{0.05}O_2$ (6, 25 °C)	50, 0.1C, 109.1 (70 MPa)	39, 0.1C, micro short-circuit	LPSC	72
	Li–Al–Cl stratified structure	700 h, 0.5, 0.5	2.5, —	160 h, 0.5, 0.5	$LiNi_{0.83}Co_{0.12}Mn_{0.05}O_2$ (NCM83125) (1.78, 30 °C)	300, 0.89 mA cm^{-2}, 1.2 mAh cm^{-2} (6 MPa)	80, 0.89 mA cm^{-2}, short-circuit	LPSC	73
	Li@LCP-Cu	700 h, 1.0, 1.0	—	600 h, 1.0, 1.0	NCM811 (8.65, 25 °C)	200, 2C, 158.4	200, 2C, ~50	PEO/PVDF gel	75
	3D printed CuO-Cu	25 h, 0.05/0.1/0.2, —	—	~11 h, 0.05, —	— (—, —)	— (—)	—	LATP	76
	Ni foam	700 h, 0.2, —	0.3, —	100 h, 0.2, —	LFP (~2, 90 °C)	200, 0.2C, 135	70, 0.2C, ~10	SPE-(LLZTO)-SPE	77
	Porous SSE with ALD ZnO	300 h, 0.5, 1.0	—	—	— (—, —)	— (λ)	—	LLCZN	78
	VGCM@Li	120 h, 0.5, —	—	60 h, 0.5, —	NCM523 (—, 25 °C)	50, 0.5C, 117.6 (—)	25, 0.5C, failed	PVDF-LLZTO	87
	Li/NA (Cu_3N NWs)	3000 h, 0.1, 0.1	1.8, 1.8	500 h, 0.1, 0.1	LFP (2, 25 °C)	2000, 0.5C, ~100 (0.6895 MPa)	500, 0.5C, ~100	LLZTO	88
	Cu@SnNi-Li	—	—	—	LFP (2, 60 °C)	200, 1C, 129.5 (—)	30, 1C, short-circuit	PEO	89
	$LiAlCl_4$	500 h, 3.0, 3.0	—	10 h, 0.5, 0.5	$LiCoO_2$ (LCO) (—, —)	100, 0.3C, ~90 700, 1C, ~60 (~1.5 Tons)	—	LPSC	90
	ALCP@Li (Ag/$LiNO_3$ on carbon paper)	—	2.4, 2.4	—	NCM622 (3.82, 25 °C)	50, 0.5C, 86.8 (<60 MPa)	50, 0.5C, 24	Li_3InCl_6 and $Li_{5.5-x}Ag_xPS_{4.5}Cl_{1.5}$ double-layer SSE	92
	3D porous Cu	500 h, 0.05, —	—	~430 h, 0.05, —	NCM622 (2.8, 25 °C)	80, 0.1C, 143 (35 MPa)	17, 0.1C, 40	LATP	93
	3D porous Zn layer	300 h, 0.5, 0.25	2 0, —	—	NCM523 (4.9, 25 °C)	170, 0.1C, 143.8 (30 MPa)	—	LLZTO	94
	LiRLIA	1000 h, 5.0, 0.5 950 h, 0.5, 5.0	—	90 h, 0.5, 1.0	LFP (2.5, 60 °C)	2000, 5C, 125 (—)	2000, 5C, 66.2	PEGDME	91
	Li-10%SnF_2	300 h, 0.5, 0.5	3.5, 3.5	10 h, 0.5, 0.5	$LiNi_{0.7}Co_{0.1}Mn_{0.2}O_2$ (NCM712) (~2, —)	80, 0.2C, 133.2/500, 0.5C, ~90 (—)	80, 0.2C, 58.3 500, 0.5C, ~20	$LSPCl_{1.5}$	95
	Pre In anode	2000 h, 2.55, —	2.55, —	—	LCO (—, 25 °C)	700, 0.5C, ~110 (25.48 mg cm^{-2})/100, 0.1C, ~110 (38.21 mg cm^{-2}) (120 MPa)	—	LPSC	102

Table 1 *(Contd.)*

Materials	Configuration	Symmetric cell (cycle, current density [mA cm^{-2}], capacity [mAh cm^{-2}])	CCD [mA cm^{-2}], capacity [mAh cm^{-2}]	Symmetric cell with planar LMA	Cathode (loading [mg cm^{-2}], working temperature)	Full cell (cycles, current density [mA g^{-1}], capacity [mAh g^{-1}] (stack pressure))	Full cell with planar LMA	Electrolyte	Ref.
Other materials	3D-SSE (LLZTO)	500 h, 0.5, —	0.7, —	5 h, 0.5, —	NCM523 (1.6 mAh cm^{-2}, 40 °C)	50, 0.2C, ~1.0 mAh cm^{-2} (1.0 MPa)	—	LLZTO	64
	Porous SSE with ALD ZnO	150 h, 0.5, —	—	—	NCM523 (14, —)	~27, 0.1C, ~170 (—)	—	Ca and Nb doped LLZO	66
	NCN-CPE (3D nanowires-bulk ceramic-nanowires)	600 h, 0.1, 0.1	—	~270 h, 0.1, 0.1	LFP (~1.2, 40 °C)	500, 0.2C, 137.3 (—)	500, 0.2C, 86.5	$Li_{6.5}La_3Zr_{1.5}Ta_{0.5}O_{12}$	67
	p-3DSE Li	2600 h, 0.5, 0.5/600 h, 1, 1	1.92, 1.92	~180 h, 1, 1	NCM811 (~22, 25 °C)	300, 0.2C, 3.19 mAh cm^{-2} (—)	—	LLZTO	68
	3D-printed LLZTO/poly (PEGDA)								
	MIEC-Ta-LLZ-MIEC	560 h, 20–60, 10–30	100, 50	—	NCM622 (2.3 mAh cm^{-2}, 25 °C)	350, 1.15, 70 (without external pressure)	—	Ta-LLZO	69
	I-Li@SPE	400 h, 0.5, 0.5	1.0, 0.5	~150 h, 0.5, 0.5 with high fluctuating voltage profiles	LFP (2.5–3.5, 60 °C)	130, 0.5C, 119 (—)	130, 0.5C, 48	PEO	74
	LiB-TFA (Li_5B_4)	6000 h, 0.5, 2/1500 h, 0.5, 10	5.8, —	88 h, 0.5, 2	FeS_2 (—, 80 °C),	420, 1C, ~550 (2.17 mAh cm^{-2})/800, 3C, ~600 (1.18 mAh cm^{-2}) (40 MPa)	~10, 1C, short-circuit (2.17 mAh cm^{-2})	LPSC	100
	80LiB@AgC	1800 h, 0.5, 2	2.7, 1	110 h, 0.5, 2	S@C (1.3(1.5 mAh cm^{-2}), 60 °C)	60, 0.2C, 1080 (13 MPa)	18, 0.2C, short-circuit	LSPSC	96
	PEO-DLSL	1000 h, 0.5, 0.5	>1, —	~30 h, 0.5, 0.5	LFP (~2.4, 60 °C)	1000, 0.5C, ~125 (—)	70, 0.5C, short-circuit	PEO-SPE	97
	SC-SiN	600 h, 15, 0.25	12, 0.25	~15, 15, 0.25	LCO (2.7 mAh cm^{-2}, 55 °C)	600, 5.4, ~100 (250 MPa)	—	LPSC	98
	Li/graphite (G)-SEs-SiG	—	—	—	NMC83 (15, 55 °C),	6000, 5C, ~96 (at 25 MPa for the pouch cell)	—	$LPSCl_{1.5}$/LGPS	99
	3D LSLL	700 h, 1.3, 0.65	>13, 0.25	—	LFP (~1.6, 30 °C)	300, 2C, ~100 (0.5 MPa)	140, 2C, ~40	LPSC	101

4.2 Mechanical rolling and pressing

Mechanical compression methods circumvent thermal processing but are limited to fabricating composite anodes with specific architectures. Tu *et al.* engineered a hybrid LiSnC electrode *via* thermocompression rolling (Fig. 6c), where Li, MCMB, and Sn form a heterogeneous composite.[72] The $Li_{22}Sn_5$ lithiophilic seeds embedded in the LiC_6 skeleton extend electrochemical reactions from the surface to the bulk phase, enabling symmetric cells to achieve 400 h cycling at 0.5 mA cm^{-2}. This demonstrates the material versatility of mechanical compression in 3D electrode design. In addition, mechanical pressing can also achieve full mixing of lithium and skeleton materials based on a wound multilayer structure. Mechanical rolling and pressing methods can also be used to prepare special structured electrodes through process control. Tu *et al.* deposited nanoscale $AlCl_3$ on Li foil, constructing a Li–Al–Cl stratified architecture through iterative winding and roller compaction (Fig. 6d).[73] Pressure-induced atomic diffusion forms continuous Li/Li_9Al_4 and Li/LiCl interfaces, with Li_9Al_4 critically stabilizing the sulfide SSE/LMA interface. Cui *et al.* advanced this paradigm by pressing Li foil with a PE@PEO-based polymer electrolyte layer, then spiral-winding it into an interdigitated Li@solid-polymer-electrolyte (I-Li@SPE) framework (Fig. 6e).[74] This transforms planar SSE-Li contacts into 3D interlocking interfaces, reducing the local current density by 60% *via* COMSOL simulation and enhancing the high-rate cyclability. The method offers scalable, controllable manufacturing. The traditional roller pressing method cannot achieve the preparation of thin lithium foil with high mechanical strength and low lithium content. Han *et al.* developed a fast and simple hot pressing method to achieve an ultra-low lithium metal content 3D lithiophilic carbon paper/copper current collector hybrid anode (Li@LCP-Cu) with a thickness of ~100 μm (Fig. 6f).[75] The raw samples were arranged from top to bottom in the order of Cu foil, Li metal, carbon paper, and the second Cu foil, and the preparation of the ultra-thin 3D Li@LCP-C anode was achieved by regulating temperature, time, and pressure. The stable lithiophilic LiC_x layer formed *in situ* provides abundant nucleation sites and reduces the nucleation overpotential of LMA. The 3D scaffold concurrently mitigates volume fluctuation and electrode pulverization during cycling.

4.3 3D printing

3D printing technology pioneers geometric architecture optimization of lithium metal anodes through adaptive molding and solidification of functional inks. This emerging approach enables *in situ* construction of 3D conductive scaffolds directly on solid electrolytes.[56,80,81] Based on the guidance of 3D printing technology and machine learning, Sierros *et al.* demonstrated this by fabricating patterned porous Cu frameworks on $Li_{1+x}Al_xTi_{2-x}(PO_4)_3$ (LATP) electrolyte interfaces (Fig. 6g), achieving unprecedented solid–solid interfacial contact in ASSLBs.[76] While current equipment limitations warrant further investigation, the integration of machine learning with

3D printing unlocks transformative potential for guided electrode architecture design.

5. Materials matrices of 3D LMA

Researchers have engineered 3D LMAs utilizing carbon-based, metal-based, and other composite-based scaffolds for liquid electrolyte systems, achieving significant improvements in dendrite suppression and solid electrolyte interphase (SEI) stability. However, these strategies face substantial challenges when extended to SSBs. The absence of electrolyte fluidity necessitates intricate designs for unobstructed ion/electron transport channels to ensure stable LMA operation, with this complexity compounded by interfacial incompatibility and stress accumulation at the interface. The scaffold architecture for 3D LMAs has evolved through three key stages: single-component scaffolds, binary synergistic and finally multicomponent coupled systems. Early single-component scaffolds (*e.g.*, porous Cu/Ni foam) offered basic physical hosting and electron conduction but suffered from poor interfacial contact and mechanical weakness. Binary synergistic scaffolds (*e.g.*, metal–ceramic composites) overcame these by complementary design, merging conductivity with ion flux homogenization to raise the CCD. The emerging multicomponent scaffolds (*e.g.*, metal/ceramic/polymer systems) synergistically combine gradient materials, polymers, and conductive networks. This achieves homogeneous ion distribution and signifies a paradigm shift from passive lithium hosting to intelligent active regulation. Crucially, the SSE itself can serve as a structural scaffold to direct Li deposition. Its inherent rigidity enables confinement of Li within subsurface pores and grain boundaries, thereby guiding non-planar deposition morphologies. This paradigm has spurred extensive exploration of electrolyte-as-host architectures for 3D anode construction.

5.1 Carbon-based materials

Carbon-based materials are widely employed in constructing 3D composite lithium anodes due to their light weight nature and structural stability. These scaffolds are categorized into pure carbon frameworks (*e.g.*, porous carbon,[82] graphite,[83] CF,[55] carbon nanotubes (CNTs),[61,84] graphene[85]) and carbon composite systems (*e.g.*, C/Si,[62] C/Li_3N,[58] C/metals). Dörfler *et al.* engineered commercial porous carbon (YP-50F) through ethane-based chemical vapor deposition (CVD) and constructed it as a 3D scaffold for LMA (Fig. 7a).[82] In half-cell tests using the LPSC electrolyte, the coulombic efficiency was improved from 55.3% to 79.5%. This indicates that the host can effectively mitigate interfacial side reactions between the LMA and the sulfide electrolyte. Carbon-based materials generally exhibit high electronic conductivity. However, their ionic conductivity severely limits their practical utility. Consequently, an ideal 3D host must therefore be a MIEC. Liu *et al.* developed a lithium-free hybrid anode by integrating graphite with an LPS electrolyte (Fig. 7b), creating a spatially confined 3D host that directs Li deposition into the voids of a MIEC network, suppressing dendrites and mitigating short-circuit risks.[83] The unique lithium deposition behavior, enabled by the high electronic conductivity of graphite and the high ionic conductivity of LPS, combined with the large specific surface area of the 3D structure, resulted in a significant increase in the CCD from 0.4 mA cm^{-2} to 1.4 mA cm^{-2}. Wang *et al.* utilized CNT scaffolds to regulate the electrode mass-transport conductivity with the SSE of Li_7N_2I (LNI) (Fig. 7c).[84] Experimental and simulation analyses revealed that balanced lithiophobicity, triple-phase conductivity (ionic/electronic/porous), and interlayer porosity enable stable Li plating/stripping. This underscores that constructing efficient MIECs requires precise optimization of multidimensional parameters. Ultimately, Li/LNI-5% CNT achieved a critical current density of 4 mA cm^{-2} at 4 mAh cm^{-2}.

To address the mechanical instability of LMAs, pure carbon scaffolds are frequently integrated with functional materials to construct stable 3D LMAs. Li *et al.* engineered a MIEC interlayer comprising Si nanoparticles and CNTs, where the inherent lithiophilicity of Si promotes uniform nucleation while CNTs enable long-range electron transport.[62] This design spatially confines Li deposition between the current collector and the interlayer, preventing direct contact with the SSE as shown in Fig. 7d. Zhang *et al.* developed a LiMg alloy/graphite composite anode where Mg alloying suppresses pore formation, and the graphite matrix provides fast Li^+ transport pathways.[86] The $Li_{0.95}Mg_{0.05}$-50 wt% graphite anode (LM_5G_{50}) achieved a stripping capacity of 14.2 mAh cm^{-2} with 85% lithium utilization.

5.2 Metal-based materials

Metallic scaffolds offer superior electrical conductivity and mechanical strength, significantly enhancing lithium anode tolerance to high-volume fluctuations. These hosts are categorized into three classes of pure metal frameworks (*e.g.*, Cu,[87] Ni,[53] In,[91] Al,[90] Ag,[92] Ti,[52] Mg,[86]), metal-based oxides/nitrides (*e.g.*, Cu_3N[88]), alloys (*e.g.*, Cu@SnNi[90]), and metallizable precursors capable of *in situ* reduction to metallic matrices.

As the commercial current collector of choice, Cu has been extensively explored in constructing 3D anodes for ASSLBs. Fan *et al.* synthesized vertical graphene on a 3D Cu mesh (VGCM) *via* a CVD reaction (Fig. 8a), achieving symmetric cell stability >500 cycles at a current density of 5 mA cm^{-2}.[87] Guo *et al.* engineered 3D porous Cu through ammonia-induced dissolution, pairing it with an *in situ* polymerized sealant to enable stable Li deposition/stripping in the LATP electrolyte.[93] The stabilized interface yielded 500 h cycling lifespan, while full cells with $LiNi_{0.6}Co_{0.2}Mn_{0.2}O_2$ (NCM622) cathodes exceeded 100 cycles *versus* ~5 cycles for controls. Beyond Cu, structural metals demonstrate robust scaffolding capabilities. Lithium alloying emerges as a potent dendrite suppression strategy.[26] Other metals (Zn, Al, Mg, In, *etc.*) enhance SSE/lithium wettability while providing deposition templates. He *et al.* leveraged porous Zn carriers to deposit Li, where the 3D Li–Zn layer reduced the interfacial resistance of LLZTO/Li.[94] The gradient porous framework accelerated Li^+ kinetics and

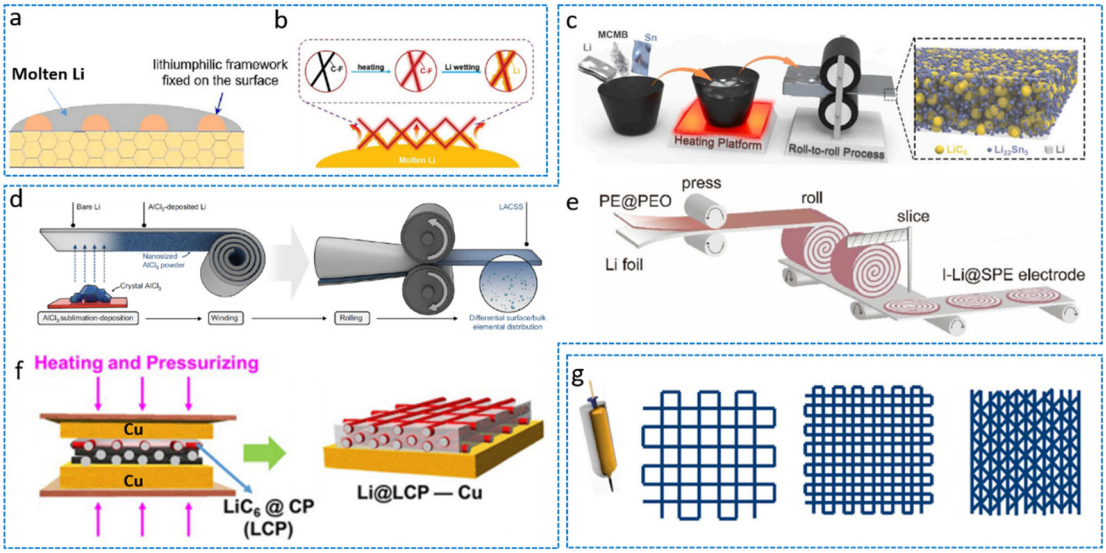

Fig. 6 Key fabrication strategies for 3D lithium metal anodes. (a) Molten Li wetting on the LLZTO electrolyte demonstrates enhanced interfacial compatibility for hybrid architectures.[71] Reproduced with permission from Elsevier, copyright 2023. (b) Molten Li infusion into CF scaffolds achieves conformal Li/CF composites through capillary-driven filling.[55] Reproduced with permission from John Wiley & Sons, copyright 2019. (c) Mechanical alloying synthesizes LiSnC metal matrix composites with homogeneous phase distribution.[72] Reproduced with permission from Elsevier, copyright 2023. (d) Schematic diagram of the Li–Al–Cl stratified structure preparation process.[73] (e) Manufacturing process of I-Li@SPE.[74] Reproduced with permission from John Wiley & Sons, copyright 2022. (f) Fabrication of the hybrid Li@LCP-Cu anode by the host-pressing method.[75] Reproduced with permission from Elsevier, copyright 2023. (g) Diagrams of printing patterns for various scaffolds.[76] Reproduced with permission from Elsevier, copyright 2021.

prevented filamentous growth, elevating CCD to 2.0 mA cm^{-2} *versus* 0.1 mA cm^{-2} for bare Li. Notably, lithiophilic metals enable selective Li deposition. Sun *et al.* designed 3D Li-rich $Li_{13}In_3$ alloy electrodes (LiRLIA) to suppress dendrites under a high current density.[91] The $Li_{13}In_3$ substrate exhibited stronger Li adsorption energy and lower diffusion barrier *versus* pure Li, directing confined Li deposition within scaffolds. Consequently, symmetric cells were operated for about 1000 h at a high current density/capacity of 5 mA cm^{-2}/5 mAh cm^{-2}. While alloying effectively modulates deposition behavior, metallic scaffolds inherently reduce the cell operational voltage, compromising the energy density of batteries.

Despite the widespread adoption of monolithic metallic scaffolds, their intrinsic rigidity often impedes the optimal interfacial conformity with SSEs. Beyond interfacial limitations, single-component systems exhibit inadequate precision in regulating the Li^+ flux distribution and deposition morphology. To overcome these constraints, contemporary research prioritizes metal compound/alloy hybrids as multifunctional Li hosts. Mai *et al.* engineered lithiophilic nanotrenches (Li/NA) *via* Cu_3N nanowire arrays on SSE surfaces.[88] During initial cycling, the *in situ* conversion reaction generates Cu-Li_3N nanocomposites that establish continuous ion-conducting pathways (Fig. 8b). This transformation homogenizes the electric field distribution while slashing the interfacial resistance from 36 to 4 Ω cm^{-2}, effectively suppressing dendritic propagation through interfacial densification. Yao *et al.* constructed a Sn/Ni alloy layer-coated Cu nanowire (Cu@SnNi) network on the anode side, and the lithiated alloy creates low-barrier Li^+ migration channels, directing preferential Li deposition onto nanowire surfaces rather than inter-wire voids (Fig. 8c).[89] This spatially confined deposition enabled stable cycles of more than 200 times in full cells with $LiFePO_4$ cathodes, demonstrating exceptional interfacial stability under practical cycling conditions. Similarly, Yu *et al.* used SnF_2 to compound Li in the molten state.[95] The roll-pressing process with Li triggers the reaction of SnF_2 generating $Li_{22}Sn_5$ with LiF matrices *in situ*. It was experimentally demonstrated that with the amount of SnF_2 up to 10%, the CCD of the Li-10% SnF_2/$Li_{5.5}PS_{4.5}Cl_{1.5}$ ($LSPCl_{1.5}$)/Li-10%SnF_2 symmetric cell can reach 3.5 mA cm^{-2}. The *in situ* formed LiF effectively seals subsurface pores, while $Li_{22}Sn_5$ provides lithiophilic nucleation sites, collectively enhancing interfacial ion transfer kinetics. Sun *et al.* used the lithiation reaction during the initial cycling to react $LiAlCl_4$ with Li to form LiAl alloys as the 3D skeleton (Fig. 8d).[90] The resulting LiAl alloy layer forms intimate interfaces with both Li metal and LPSC, functioning as the structural buffer mitigating volume fluctuations, reactive barrier preventing continuous SEI reformation and the lithiophilic guide reducing nucleation overpotential. Consequently, the symmetric cells achieved unprecedented 500 h cycling at 3 mA cm^{-2}, which highly exceeds conventional metallic scaffolds.

5.3 Other composite materials

While metallic porous scaffolds offer robust mechanical support, their high mass density compromises the intrinsic energy density advantage of lithium metal anodes. By contrast, non-metallic lithiophilic materials (*e.g.*, Si_3N_4,[98] Li_5B_4,[100] *etc.*)

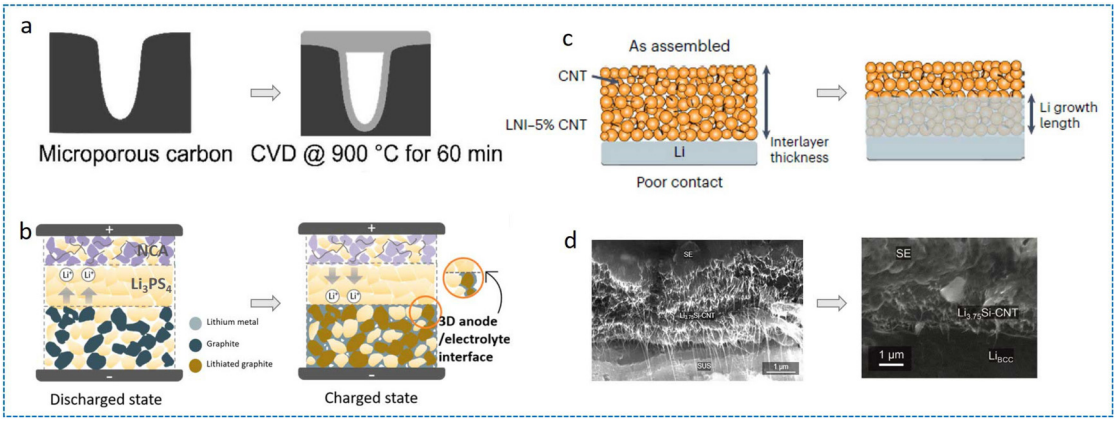

Fig. 7 (a) CVD coating process in microporous carbon.[82] (b) Working mechanisms of the graphite-based lithium-free 3D hybrid anode.[83] Reproduced with permission from American Chemical Society, copyright 2021. (c) Li can nucleate on the Li/LNI-CNT interface rather than the SSE/LNI-CNT interface.[84] Reproduced with permission from Springer Nature, copyright 2024. (d) SEM images of the $Li_{3.75}Si$-CNT interlayer and the interlayer after Li deposition.[62]

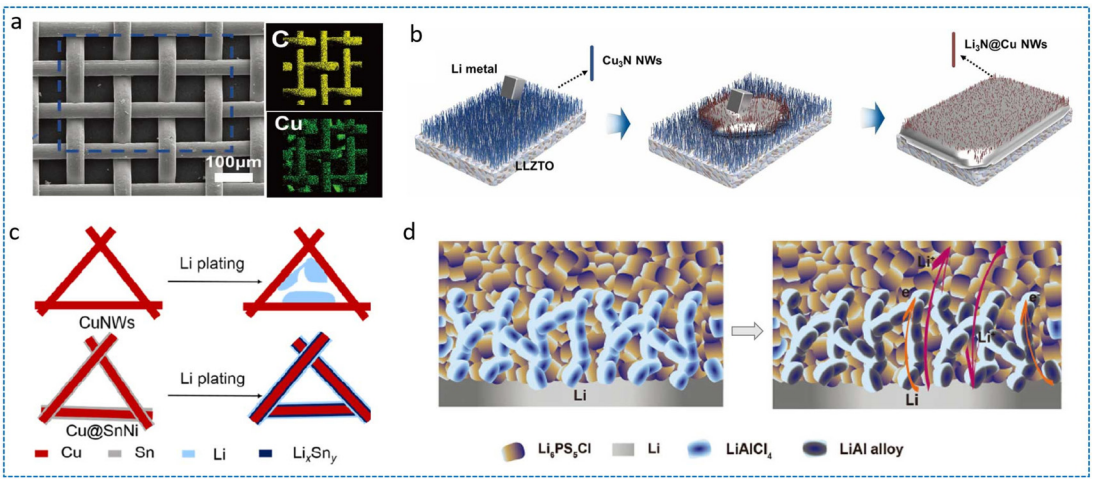

Fig. 8 (a) SEM image and EDS mapping of VGCM.[87] Reproduced with permission from John Wiley & Sons, copyright 2019. (b) The evolution of Cu_3N nanowires with molten Li dropped on the electrolyte surface.[88] Reproduced with permission from American Chemical Society, copyright 2024. (c) Plating behavior of Li metal in CuNWs and Cu@SnNi networks.[89] Reproduced with permission from American Chemical Society, copyright 2019. (d) The formation of a Li–Al alloy in 3D LMA with the reaction between the halide electrolyte and Li metal during the remaining process.[90]

exhibit reduced Li nucleation barriers, promoting homogeneous deposition at nanoscale sites. Precise Li regulation in 3D LMAs is typically achieved through elemental doping or *in situ* alloying reactions. Notably, structural engineering of SSEs can inherently create 3D architectures accommodating Li deposition/stripping, where the SSE simultaneously functions as an ionic conductor and scaffold. Although polymer additives or lithiophilic coatings enhance Li/SSE interfacial contact (discussed in section 3), this section focuses on SSE-integrated scaffold systems.

Yang *et al.* engineered an 80LiB lithium-rich alloy scaffold with conformal Ag@C interlayers (80LiB-Ag@C) interfacing the $Li_{9.54}Si_{1.74}P_{1.44}S_{11.7}Cl_{0.3}$ (LSPSCl) electrolyte (Fig. 9a).[96] *Operando* ^{7}Li NMR revealed chemical shift evolution during discharge, confirming uniform Li deposition and suppressed interfacial reactions. As a result, the symmetric cell can achieve a stable coulombic efficiency of about 99.9% and more than 1750 cycles with 0.5 mA cm^{-2} and 2 mAh cm^{-2}. The full-cell with S as the cathode can express a specific capacity of 1316 mAh g^{-1} with 82% capacity retention after 60 cycles. Notably, silicon (Si)-based scaffolds demonstrate exceptional Li^+ storage capability. Yu *et al.* fabricated diatomite-derived porous silicon *via* magnesiothermic reduction, forming $Li_{4.4}Si$ composites subsequently encapsulated by the PEO-based solid polymer electrolyte (SPE) to form a 3D PEO-SPE-coated diatomite-derived lithium silicide-Li (PEO-DLSL) anode (Fig. 9b).[97] The hierarchical porosity accommodated the volume expansion of LMA while eliminating interfacial voids. The PEO-DLSL anode demonstrated significantly enhanced cycling stability

compared to planar Li foil under relatively demanding conditions (0.5 mA cm^{-2}, 0.5 mAh cm^{-2}); it sustained stable lithium stripping/plating for over 1000 h with minimal overpotential growth. In contrast, the planar Li-foil cell exhibited a progressive increase in voltage hysteresis due to accumulating interfacial impedance, culminating in an internal short circuit within 100 h. Wu *et al.* developed a room-temperature liquid Li-Phen-ether complex, enabling the construction of 3D LSLL anodes with dual ion/electron conduction pathways.[101] The symmetric cells can achieve critical current densities higher than 13 mA cm^{-2} and long cycle lives higher than 1000 h at 0.25 mA cm^{-2}. Further investigations by Wu *et al.* compared the compatibility of hard carbon (HC), soft carbon (SC), graphene material, and soft carbon-nano Si_3N_4 (SC-SiN) material for the LPSC electrolyte with LMA and found that the symmetric cell with SC-SiN as the Li host can achieve a high critical current density of 12 mA cm^{-2} at 0.25 mAh cm^{-2} (Fig. 9c–f).[98] Si_3N_4 will generate Li_3N *in situ* on the anode during charging and discharging processes, and the presence of Li_3N can realize fast ion transport and enhance the critical current density of the battery. Combined with LCO, SC-SiN based LMA can realize more than 22 000 stable cycles at an ultra-high current density of 12.5 mA cm^{-2}, which provides an important demonstration of the application of a 3D host in ASSLBs. Crucially, nanoscale materials inherently reduce the volumetric energy density of the battery, which is a key consideration in the 3D LMA construction. In the process of screening materials, Li *et al.* found the interfacial shrinkage sensitivity of the micrometer silicon material. Unlike the Li–Si alloy formed with the liquid-state electrolyte, the micrometer silicon in the solid-state battery only occurs in the thin layer on the surface of the alloying reaction (Fig. 9g–i).[99] The alloying reaction and this shrinkage sensitivity facilitate the establishment of an active 3D scaffold for more rapid bulk lithium deposition or stripping. The authors used a composite layer formed by micrometre-sized Si and graphite particles (SiG) as the lithium anode host, paired with a $LiNi_{0.83}Mn_{0.06}Co_{0.11}O_2$ (NMC83) anode to achieve up to 2000 stable cycles at a surface loading of 22 mg cm^{-2} with a current density of 19.5 mA cm^{-2}.

6. Challenges and perspectives

Although 3D lithium hosts demonstrate remarkable potential for ASSLBs, significant challenges must be addressed to realize their practical implementation. Overcoming these challenges requires coordinated efforts across fundamental science, materials engineering, and battery technology to bridge the gap between laboratory achievements and commercial viability for ASSLBs.

First, the fundamental failure mechanisms of lithium metal in solid-state systems remain inadequately characterized, particularly regarding dendrite nucleation and propagation through solid electrolytes. The exact nucleation and growth mechanisms differ substantially from liquid systems. The lack of suitable *in situ* characterization tools capable of probing these phenomena at relevant length and time scales represents a significant knowledge gap. Current *ex situ* techniques often fail to capture the dynamic evolution of solid–solid interfaces during cycling, particularly regarding how lithium infiltrates porous hosts and interacts with solid electrolyte particles. Developing advanced characterization platforms that combine high-resolution imaging with electrochemical measurements under realistic operating conditions should be a top research priority.

Second, a critical limitation lies in simultaneously satisfying optimal thermodynamic stability and efficient dual ion/electron conduction pathways for current 3D host materials. The ideal host must provide both electronic and ionic conduction pathways while maintaining thermodynamic stability against lithium and sufficient mechanical strength to withstand cycling stresses. Carbon-based architectures, while being light weight and electronically conductive, typically exhibit poor lithiophilicity and cannot alone facilitate uniform ion transport. Metallic scaffolds offer excellent electronic conductivity but add considerable weight and show limited ability to regulate the lithium deposition morphology. Polymer–ceramic composites and many other materials attempt to balance these properties but face challenges in creating continuous conduction networks at practical loading levels. Future materials innovation should focus on hybrid architectures that combine complementary material properties, perhaps through gradient designs or self-healing mechanisms that can adapt during battery operation.

Third, for practical high-energy-density applications, systematic optimization of electrode architectures is crucial, including: (i) ultrathin current collectors to minimize the inactive material content, (ii) mechanical reinforcement strategies to maintain structural integrity, and (iii) scalable fabrication processes. Additionally, the development of standardized testing protocols will enable meaningful comparison between different host designs. Mechanical integration challenges become particularly acute in large-format cells where maintaining uniform interfacial contact under cycling conditions is non-trivial. The mismatch in mechanical properties between rigid solid electrolytes and porous hosts can lead to contact loss and increased impedance over time. Furthermore, most current fabrication methods for 3D hosts lack the scalability required for commercial production, highlighting the need for manufacturing approaches compatible with continuous production while maintaining precise control over the host architecture.

Lastly, thermal management represents another underappreciated challenge that may become critical as current densities increase. The thermal conductivity of composite anodes and its evolution during cycling have been scarcely studied, yet localized heating effects could significantly impact both performance and safety in practical cells. This is particularly relevant for 3D hosts where the increased surface area and complex microstructure may alter heat generation and dissipation characteristics compared to planar electrodes.

For future perspectives, the field must pursue a coordinated research strategy that bridges fundamental understanding with practical implementation. The integration of computational materials design with advanced manufacturing tech-

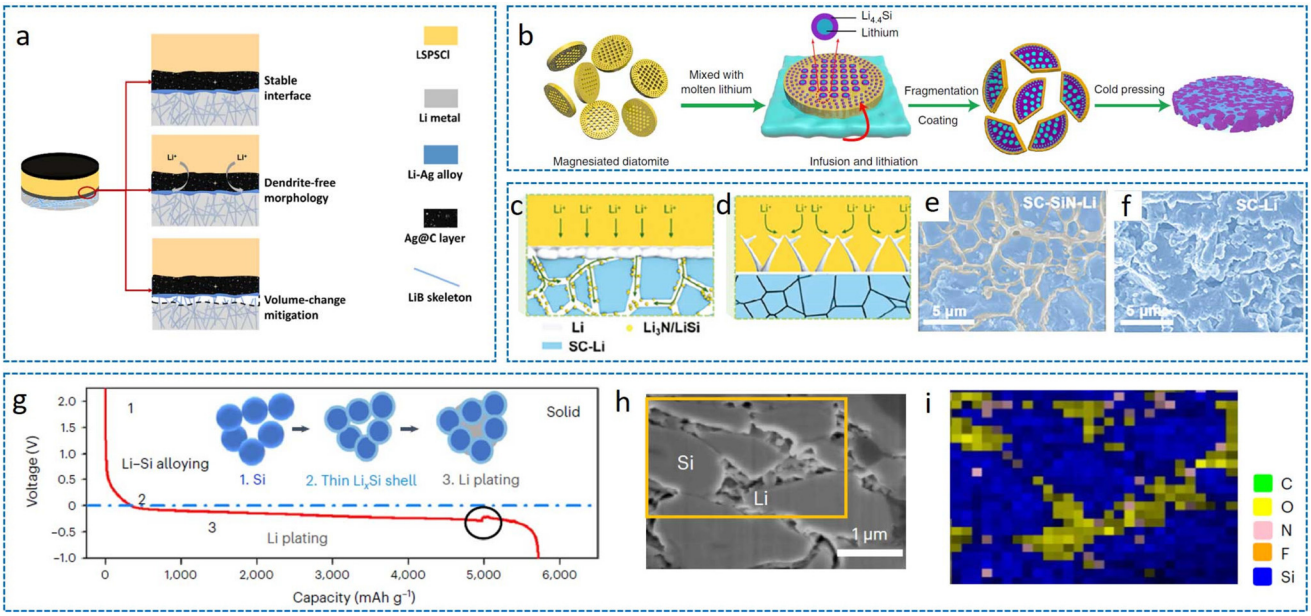

Fig. 9 (a) Working mechanism of 80LiB@AgC.[96] Reproduced with permission from American Chemical Society, copyright 2022. (b) The fabrication process of PEO-DLSL.[97] (c–f) Advantages of SC-SiN compared with SC on working as 3D LMA.[98] Reproduced with permission from John Wiley & Sons, copyright 2024. (g) Li discharge profile in a battery of Li/graphite-LPSCl$_{1.5}$-LGPS-LPSCl$_{1.5}$-SiG at a current density of 0.2 mA cm^{-2} at room temperature and (h) FIB-SEM with (i) elemental maps of SiG-based LMA.[99] Reproduced with permission from Springer Nature, copyright 2024.

niques could accelerate the discovery of optimal host materials.[103–107] Multiscale modeling approaches like phase-field simulations may provide critical insights into lithium deposition behavior.[108] Meanwhile, the exploration of anode-free configurations using prelithiated 3D hosts could further enhance the energy density. While significant challenges remain, the great progress in characterization techniques and materials engineering approaches provides a clear pathway toward realizing the potential of 3D lithium hosts for next-generation SSBs. Success in this endeavor could finally enable the fabrication of safe, high-energy-density lithium metal batteries that have long been pursued by both academia and industry. As the 3D structures display unique advantages in the design of ASSLBs, there are also many practical issues that need to be solved. Firstly, the balance of electrode volumetric density and electrochemical performances is expected to be considered. Moreover, the weight of inactive composites inside the 3D structure should be controlled to achieve a high energy density of batteries. Afterwards, the compatibility between anode composites and the SSEs should also be taken into account while selecting the scaffold/host materials. Lastly, in order to achieve highly stable batteries, the structure tailoring of SSEs and the cathode should be carried out simultaneously.

For the creations of 3D structures, more studies need to focus on: (i) exploring the guiding principles for electron and ion transport; (ii) analyzing the failure mechanisms of 3D metal anodes in solid-state batteries to inform the design of 3D anodes; (iii) ensuring cost-effectiveness, aiming to simplify the preparation methods under multi-component conditions and enable large-scale production of 3D LMA.

7. Conclusion

In this review, we have meticulously summarized the failure mechanisms of LMAs in ASSLBs and highlighted the distinct advantages of 3D-structured anodes in mitigating dendrite initiation and propagation within solid-state systems. Through a critical evaluation of structural design principles, fabrication methodologies, and host material architectures for 3D LMAs, we have established fundamental guidelines for their rational construction. This work provides a scientific foundation for developing next-generation dendrite-free 3D LMA and identifys several critical scientific questions to be resolved in ASSLBs.

Conflicts of interest

There are no conflicts to declare.

Data availability

No primary research results, software or code have been included and no new data were generated or analysed as part of this review.

Acknowledgements

We acknowledge the financial support provided by the National Natural Science Foundation of China (Grant No. 52225105, 22279127) and the Fundamental Research Funds

for the Central Universities (WK9990000170). This work was supported by the National Key Research and Development Program of China (Grant No. 2022YFA1504102), the National Natural Science Foundation of China (Grant No. 52072358, U21A2082), the Strategic Priority Research Program of the Chinese Academy of Sciences (Grant No. XDB0450302), and the Robotic AI-Scientist Platform of the Chinese Academy of Sciences.

References

1 K. Nieto, D. S. Windsor, B. S. Vishnugopi, P. P. Mukherjee and A. L. Prieto, *Nat. Rev. Chem.*, 2025, **9**, 118–133.
2 T. Jiang, D. Shen, Z. Zhang, H. Liu, G. Zhao, Y. Wang, S. Tan, R. Luo and W. Chen, *Nat. Rev. Clean Technol.*, 2025, **1**, 474–492.
3 T. Xu, W. Sun, T. Kong, J. Zhou and Y. Qian, *Acta Phys. -Chim. Sin.*, 2024, **40**, 2303021.
4 S. Chen, X. Hu, L. Nie, Y. Yu and W. Liu, *Sci. China Mater.*, 2023, **66**, 2192–2198.
5 X. Hu, Z. J. Zhang, X. Zhang, Y. Wang, X. Yang, X. Wang, M. Fayena-Greenstein, H. A. Yehezkel, S. Langford, D. Zhou, B. H. Li, G. X. Wang and D. Aurbach, *Nat. Rev. Mater.*, 2024, **9**, 305–320.
6 Z. Zhang and W. Q. Han, *Nano-Micro Lett.*, 2024, **16**, 24.
7 X. Li, Z. Zhang, J. Feng, X. Yin, X. Cui, W. Xu, H. Zhang, R. Zeng and S. Ding, *Sci. China Mater.*, 2024, **67**, 1412–1421.
8 T. Zhou, R. Xu, X. Cao, J. Zhang, J. Wang, R. Huang, X. Ping, P. Bai, Z. Sun, M. Liu and X. Wang, *Sci. China Mater.*, 2024, **67**, 2256–2265.
9 Y. Zhao, X. Da, Y. Qin, X. Jia, X. Deng, S. Ding, J. Xiong, Q. Rong, X. Kong and G. Gao, *Sci. China Mater.*, 2024, **67**, 3994–4004.
10 J. Zou, J. Zhang, L. Wang, Q. Sun, Y. Wang, M. Zheng, H. Hu, Y. Xiao, Y. Liu and Y. Liang, *Sci. China Mater.*, 2024, **67**, 1445–1454.
11 K. Yan, H.-W. Lee, T. Gao, G. Zheng, H. Yao, H. Wang, Z. Lu, Y. Zhou, Z. Liang, Z. Liu, S. Chu and Y. Cui, *Nano Lett.*, 2014, **14**, 6016–6022.
12 W.-J. Kong, C.-Z. Zhao, L. Shen, J.-L. Li, Y.-C. Le, X.-Y. Huang, P. Xu, J.-K. Hu, J.-Q. Huang and Q. Zhang, *EES Batteries*, 2025, **1**, 1353–1370.
13 Y. Lu, C. Z. Zhao, H. Yuan, X. B. Cheng, J. Q. Huang and Q. Zhang, *Adv. Funct. Mater.*, 2021, **31**, 2009925.
14 C. H. Wang, J. T. Kim, C. S. Wang and X. L. Sun, *Adv. Mater.*, 2023, **35**, 2209074.
15 S. J. Liu, L. Zhou, T. J. Zhong, X. Wu and K. Neyts, *Adv. Energy Mater.*, 2024, **14**, 2403602.
16 J. X. Zhang, J. M. Fu, P. S. Lu, G. T. Hu, S. J. Xia, S. T. Zhang, Z. Q. Wang, Z. M. Zhou, W. L. Yan, W. Xia, C. H. Wang and X. L. Sun, *Adv. Mater.*, 2025, **37**, 2413499.
17 S. J. Chen, C. Pan, Q. L. Wang, J. L. Luo and X. Z. Fu, *Adv. Funct. Mater.*, 2024, **34**, 2409812.
18 X. Wang, Z. Chen, K. Jiang, M. H. Chen and S. Passerini, *Adv. Energy Mater.*, 2024, **14**, 2304229.
19 X. He, K. Zhang, Z. Zhu, Z. Tong and X. Liang, *Chem. Soc. Rev.*, 2024, **53**, 9–24.
20 A. Mohammadi, L. Monconduit, L. Stievano and R. Younesi, *J. Electrochem. Soc.*, 2022, **169**, 070509.
21 J. N. Chazalviel, *Phys. Rev. A*, 1990, **42**, 7355–7367.
22 L. Stolz, G. Homann, M. Winter and J. Kasnatscheew, *Mater. Today*, 2021, **44**, 9–14.
23 Z. Gu, D. Song, S. Luo, H. Liu, X. Sun, L. Zhu, W. Ma and X. Zhang, *Adv. Energy Mater.*, 2023, **13**, 2302945.
24 T. Krauskopf, B. Mogwitz, H. Hartmann, D. K. Singh, W. G. Zeier and J. Janek, *Adv. Energy Mater.*, 2020, **10**, 2000945.
25 E. J. Cheng, A. Sharafi and J. Sakamoto, *Electrochim. Acta*, 2017, **223**, 85–91.
26 K. Yan, Z. Lu, H.-W. Lee, F. Xiong, P.-C. Hsu, Y. Li, J. Zhao, S. Chu and Y. Cui, *Nat. Energy*, 2016, **1**, 16010.
27 A. Pei, G. Zheng, F. Shi, Y. Li and Y. Cui, *Nano Lett.*, 2017, **17**, 1132–1139.
28 H. J. S. Sand, *Philos. Mag.*, 1901, **1**, 45–79.
29 C.-Y. Tang and S. J. Dillon, *J. Electrochem. Soc.*, 2016, **163**, A1660–A1665.
30 C. Monroe and J. Newman, *J. Electrochem. Soc.*, 2005, **152**, A396–A404.
31 A. Yulaev, V. Oleshko, P. Haney, J. L. Liu, Y. Qi, A. A. Talin, M. S. Leite and A. Kolmakov, *Nano Lett.*, 2018, **18**, 1644–1650.
32 S. Hao, J. J. Bailey, F. Iacoviello, J. F. Bu, P. S. Grant, D. J. L. Brett and P. R. Shearing, *Adv. Funct. Mater.*, 2021, **31**, 2007564.
33 T. Krauskopf, F. H. Richter, W. G. Zeier and J. Janek, *Chem. Rev.*, 2020, **120**, 7745–7794.
34 F. Han, A. S. Westover, J. Yue, X. Fan, F. Wang, M. Chi, D. N. Leonard, N. J. Dudney, H. Wang and C. Wang, *Nat. Energy*, 2019, **4**, 187–196.
35 H. Yun, E. Lee, J. Han, E. Jang, J. Cho, H. Kim, J. Lee, B. Min, J. Lee, Y. Piao, J. Yoo and Y. S. Kim, *Adv. Energy Mater.*, 2025, **15**, 2404044.
36 T. Wang, B. Chen, Y. Liu, Z. Song, Z. Wang, Y. Chen, Q. Yu, J. Wen, Y. Dai, Q. Kang, F. Pei, R. Xu, W. Luo and Y. Huang, *Science*, 2025, **388**, 311–316.
37 C. Wang, Y. He, P. Zou, Q. He, J. Li and H. Xin, *J. Am. Chem. Soc.*, 2025, **147**, 19084–19092.
38 J. Gu, X. Chen, Z. He, Z. Liang, Y. Lin, J. Shi and Y. Yang, *Adv. Energy Mater.*, 2023, **13**, 2302643.
39 A. Banerjee, X. Wang, C. Fang, E. A. Wu and Y. S. Meng, *Chem. Rev.*, 2020, **120**, 6878–6933.
40 S. Hao, S. R. Daemi, T. M. M. Heenan, W. J. Du, M. Storm, M. Al-Hada, C. Rau, D. J. L. Brett and P. R. Shearing, *ACS Nano*, 2025, **19**, 20516–20525.
41 K. Li, J. Huang, X. Qu, G. Fu, X. Chen, W. Shen and Y. Lin, *Chem. Mater.*, 2025, **37**, 5884–5898.
42 J. Kasemchainan, S. Zekoll, D. S. Jolly, Z. Ning, G. O. Hartley, J. Marrow and P. G. Bruce, *Nat. Mater.*, 2019, **18**, 1105–1111.

43 D. X. Cao, K. A. Zhang, W. Li, Y. X. Zhang, T. T. Ji, X. H. Zhao, E. Cakmak, J. E. Zhu, Y. Cao and H. L. Zhu, *Adv. Funct. Mater.*, 2023, **33**, 2307998.
44 Z. Ning, G. Li, D. L. R. Melvin, Y. Chen, J. Bu, D. Spencer-Jolly, J. Liu, B. Hu, X. Gao, J. Perera, C. Gong, S. D. Pu, S. Zhang, B. Liu, G. O. Hartley, A. J. Bodey, R. I. Todd, P. S. Grant, D. E. J. Armstrong, T. J. Marrow, C. W. Monroe and P. G. Bruce, *Nature*, 2023, **618**, 287–293.
45 Y. Zhu, Y. Wang, M. Xu, Y. Wu, W. Tang, D. Zhu, Y.-S. He, Z.-F. Ma and L. Li, *Acta Phys.-Chim. Sin.*, 2023, **39**, 2110040.
46 S. S. Chi, Y. C. Liu, N. Zhao, X. X. Guo, C. W. Nan and L. Z. Fan, *Energy Storage Mater.*, 2019, **17**, 309–316.
47 Q. Xia, Y. Cai, W. Liu, J. Wang, C. Wu, F. Zan, J. Xu and H. Xia, *Acta Phys.-Chim. Sin.*, 2023, **39**, 2212051.
48 N. Marana, S. Casassa, M. Sgroi, L. Maschio, F. Silveri, M. D'Amore and A. M. Ferrari, *Langmuir*, 2023, **39**, 18797–18806.
49 J. Park, T. Watanabe, K. Yamamoto, T. Uchiyama, T. Takami, A. Sakuda, A. Hayashi, M. Tatsumisagoc and Y. Uchimoto, *Chem. Commun.*, 2023, **59**, 7799–7802.
50 W. Li, M. Li, S. Wang, P.-H. Chien, J. Luo, J. Fu, X. Lin, G. King, R. Feng, J. Wang, J. Zhou, R. Li, J. Liu, Y. Mo, T.-K. Sham and X. Sun, *Nat. Nanotechnol.*, 2024, **20**, 265–275.
51 J. Li, Y. Li, T. Liu, S. Zhang, X. Li and L. Ci, *Adv. Funct. Mater.*, 2025, 2504546.
52 Q. Li, T. C. Yi, X. L. Wang, H. Y. Pan, B. G. Quan, T. J. Liang, X. X. Guo, X. Q. Yu, O. W. R. Wang, X. J. Huang, L. Q. Chen and H. Li, *Nano Energy*, 2019, **63**, 103895.
53 S. H. Park, D. Jun, G. H. Lee, S. G. Lee, J. E. Jung, K. Y. Bae, S. Son and Y. J. Lee, *Adv. Sci.*, 2022, **9**, 2203130.
54 Z. Q. Wang, X. Y. Li, Y. M. Chen, K. Pei, Y. W. Mai, S. L. Zhang and J. Li, *Chem*, 2020, **6**, 2878–2892.
55 Y. Zhang, Y. Shi, X.-C. Hu, W.-P. Wang, R. Wen, S. Xin and Y.-G. Guo, *Adv. Energy Mater.*, 2019, **10**, 1903325.
56 X. Gao, X. Yang, K. Adair, J. Liang, Q. Sun, Y. Zhao, R. Li, T.-K. Sham and X. Sun, *Adv. Funct. Mater.*, 2020, **30**, 2005357.
57 C. Xie, M. Rong, Q. Guo, Z. Wei, Z. Chen, Q. Huang and Z. Zheng, *Adv. Mater.*, 2024, **36**, 2406368.
58 W. Z. Cao, W. M. Chen, M. Lu, C. Zhang, D. Tian, L. Wang and F. Q. Yu, *J. Energy Chem.*, 2023, **76**, 648–656.
59 Z. Wang, X. Li, Y. Chen, K. Pei, Y.-W. Mai, S. Zhang and J. Li, *Chem*, 2020, **6**, 2878–2892.
60 J. Liu, L. Wang, Y. Cheng, M. Huang, L. Zhao, C. Zheng, W. Li, H. Gao, Z. Li, Z. Wen, G. Luo, Z. Gong, Y. Yang and M.-S. Wang, *Adv. Mater.*, 2025, **37**, 2418720.
61 S. Xu, D. W. McOwen, C. Wang, L. Zhang, W. Luo, C. Chen, Y. Li, Y. Gong, J. Dai, Y. Kuang, C. Yang, T. R. Hamann, E. D. Wachsman and L. Hu, *Nano Lett.*, 2018, **18**, 3926–3933.
62 J. Sung, S. Y. Kim, A. Harutyunyan, M. Amirmaleki, Y. Lee, Y. Son and J. Li, *Adv. Mater.*, 2023, **35**, 2210835.
63 L. Zhang, H. F. Zheng, B. Liu, Q. S. Xie, Q. L. Chen, L. Lin, J. Lin, B. H. Qu, L. S. Wang and D. L. Peng, *J. Energy Chem.*, 2021, **57**, 392–400.
64 R. Xu, F. Liu, Y. S. Ye, H. Chen, R. R. Yang, Y. X. Ma, W. X. Huang, J. Y. Wan and Y. Cui, *Adv. Mater.*, 2021, **33**, 2104009.
65 K. Fu, Y. H. Gong, G. T. Hitz, D. W. McOwen, Y. J. Li, S. M. Xu, Y. Wen, L. Zhang, C. W. Wang, G. Pastel, J. Q. Dai, B. Y. Liu, H. Xie, Y. G. Yao, E. D. Wachsman and L. B. Hu, *Energy Environ. Sci.*, 2017, **10**, 1568–1575.
66 B. Y. Liu, L. Zhang, S. M. Xu, D. W. McOwen, Y. H. Gong, C. P. Yang, G. R. Pastel, H. Xie, K. Fu, J. Q. Dai, C. J. Chen, E. D. Wachsman and L. B. Hu, *Energy Storage Mater.*, 2018, **14**, 376–382.
67 R. Fan, W. C. Liao, S. X. Fan, D. Z. Chen, J. N. Tang, Y. Yang and C. Liu, *Adv. Sci.*, 2022, **9**, 2104506.
68 Y. B. Mu, S. X. Yu, Y. Z. Chen, Y. Q. Chu, B. K. Wu, Q. Zhang, B. B. Guo, L. F. Zou, R. J. Zhang, F. H. Yu, M. S. Han, M. Lin, J. L. Yang, J. M. Bai and L. Zeng, *Nano-Micro Lett.*, 2024, **16**, 86.
69 G. V. Alexander, C. M. Shi, J. O'Neill and E. D. Wachsman, *Nat. Mater.*, 2023, **22**, 1136–1143.
70 H. Liu, M. Zhao, X. Bai, P. Wang, X. Wang and J. Li, *Etransportation*, 2023, **16**, 100234.
71 Y. Shi, Y. Cai, J. Zhao, T. Wu, X. Xue, T. Lin, P. Lin, C. Wang and H. Peng, *Chem. Eng. J.*, 2023, **469**, 144090.
72 J. Li, H. Su, Z. Jiang, Y. Zhong, X. Wang, C. Gu, X. Xia and J. Tu, *Acta Mater.*, 2023, **244**, 118592.
73 H. Su, J. Li, Y. Zhong, Y. Liu, X. Gao, J. Kuang, M. Wang, C. Lin, X. Wang and J. Tu, *Nat. Commun.*, 2024, **15**, 4202.
74 Y. Yang, H. Chen, J. Wan, R. Xu, P. Zhang, W. Zhang, S. T. Oyakhire, S. C. Kim, D. T. Boyle, Y. Peng, Y. Ma and Y. Cui, *Adv. Energy Mater.*, 2022, **12**, 2201160.
75 K. Wang, Y. Chen, L. Zhang, Q. Zhang, Z. Cheng, Y. Su, F. Shen and X. Han, *J. Mater. Sci. Technol.*, 2023, **153**, 32–40.
76 D. Cipollone, H. Yang, F. Yang, J. Bright, B. Liu, N. Winch, N. Wu and K. A. Sierros, *J. Mater. Process. Technol.*, 2021, **295**, 117159.
77 S.-S. Chi, Y. Liu, N. Zhao, X. Guo, C.-W. Nan and L.-Z. Fan, *Energy Storage Mater.*, 2019, **17**, 309–316.
78 C. Yang, L. Zhang, B. Liu, S. Xu, T. Hamann, D. McOwen, J. Dai, W. Luo, Y. Gong, E. D. Wachsman and L. Hu, *Proc. Natl. Acad. Sci. U. S. A.*, 2018, **115**, 3770–3775.
79 S. Xu, D. W. McOwen, L. Zhang, G. T. Hitz, C. Wang, Z. Ma, C. Chen, W. Luo, J. Dai, Y. Kuang, E. M. Hitz, K. Fu, Y. Gong, E. D. Wachsman and L. Hu, *Energy Storage Mater.*, 2018, **15**, 458.
80 N. Fonseca, S. V. Thummalapalli, S. Jambhulkar, D. Ravichandran, Y. Zhu, D. Patil, V. Thippanna, A. Ramanathan, W. Xu, S. Guo, H. Ko, M. Fagade, A. M. Kannan, Q. Nian, A. Asadi, G. Miquelard-Garnier, A. Dmochowska, M. K. Hassan, M. Al-Ejji, H. M. El-Dessouky, F. Stan and K. Song, *Small*, 2023, **19**, 2302718.
81 L. Wang, C. Yi, J. Luo, Z. Zhang, H. Li, L. Chen and F. Wu, *Mater. Sci. Eng., R*, 2025, **166**, 101053.
82 S. Morseburg, T. Boenke, K. Henze, K. Schutjajew, J. Kunigkeit, S. L. Benze, S. Cangaz, J. Sann, F. Hippauf, S. Dörfler, T. Abendroth, H. Althues, M. Oschatz,

E. Brunner, J. Janek and S. Kaskel, *Carbon*, 2025, **232**, 119821.
83 X. Xing, Y. Li, S. Wang, H. Liu, Z. Wu, S. Yu, J. Holoubek, H. Zhou and P. Liu, *ACS Energy Lett.*, 2021, **6**, 1831–1838.
84 Z. Wang, J. Xia, X. Ji, Y. Liu, J. Zhang, X. He, W. Zhang, H. Wan and C. Wang, *Nat. Energy*, 2024, **9**, 251–262.
85 H. Shi, M. Pei, S. Wang, F. Yao, Y. Xia, Z. Xu, S. Liu, R. Shao, W. Wang and S. Liang, *Adv. Mater. Technol.*, 2023, **8**, 2200256.
86 Z.-X. Wang, Y. Lu, C.-Z. Zhao, W.-Z. Huang, X.-Y. Huang, W.-J. Kong, L.-X. Li, Z.-Y. Wang, H. Yuan, J.-Q. Huang and Q. Zhang, *Joule*, 2024, **8**, 2794–2810.
87 S. Huang, H. Yang, J. Hu, Y. Liu, K. Wang, H. Peng, H. Zhang and L.-Z. Fan, *Small*, 2019, **15**, 1904216.
88 C. Shen, M. Yan, X. Liao, R. Xu, H. Wang, W. Feng, W. Yang, Y. Li, C. Zhou, H. Wang, X. Xu and L. Mai, *ACS Nano*, 2024, **18**, 5068–5078.
89 Z. Zhu, L.-L. Lu, Y. Yin, J. Shao, B. Shen and H.-B. Yao, *ACS Appl. Mater. Interfaces*, 2019, **11**, 16578–16585.
90 H. Duan, C. Wang, R. Yu, W. Li, J. Fu, X. Yang, X. Lin, M. Zheng, X. Li, S. Deng, X. Hao, R. Li, J. Wang, H. Huang and X. Sun, *Adv. Energy Mater.*, 2023, **13**, 2300815.
91 X. J. Gao, X. F. Yang, M. Jiang, M. T. Zheng, Y. Zhao, R. Y. Li, W. F. Ren, H. Huang, R. C. Sun, J. T. Wang, C. V. Singh and X. L. Sun, *Adv. Funct. Mater.*, 2023, **33**, 2209715.
92 Z. K. Wu, C. Yu, C. C. Wei, Z. L. Jiang, C. Liao, S. Chen, S. Q. Chen, L. F. Peng, S. J. Cheng and J. Xie, *Chem. Eng. J.*, 2023, **466**, 143304.
93 S.-Y. Li, W.-P. Wang, S. Xin, J. Zhang and Y.-G. Guo, *Energy Storage Mater.*, 2020, **32**, 458–464.
94 Z. Wan, K. Shi, Y. Huang, L. Yang, Q. Yun, L. Chen, F. Ren, F. Kang and Y.-B. He, *J. Power Sources*, 2021, **505**, 230062.
95 C. Wei, C. Liu, Y. Xiao, Z. Wu, Q. Luo, Z. Jiang, Z. Wang, L. Zhang, S. Cheng and C. Yu, *Adv. Funct. Mater.*, 2024, **34**, 2314306.
96 Z. Chen, Z. Liang, H. Zhong, Y. Su, K. Wang and Y. Yang, *ACS Energy Lett.*, 2022, **7**, 2761–2770.
97 F. Zhou, Z. Li, Y.-Y. Lu, B. Shen, Y. Guan, X.-X. Wang, Y.-C. Yin, B.-S. Zhu, L.-L. Lu, Y. Ni, Y. Cui, H.-B. Yao and S.-H. Yu, *Nat. Commun.*, 2019, **10**, 2482.
98 Z. Wang, Z. Mu, T. Ma, W. Yan, D. Wu, Y. Li, M. Yang, J. Peng, Y. Xia, S. Shi, L. Chen, H. Li and F. Wu, *Adv. Energy Mater.*, 2024, **14**, 2400003.
99 L. Ye, Y. Lu, Y. Wang, J. Li and X. Li, *Nat. Mater.*, 2024, **23**, 244–251.
100 X. X. Zhang, H. L. Yu, L. B. Ben, G. J. Cen, Y. Sun, L. P. Wang, J. F. Hao, J. Zhu, Q. F. Sun, R. H. Qiao, X. Y. Yao, H. Zhang and X. J. Huang, *Adv. Mater.*, 2025, **37**, 2506298.
101 D. Wu, J. Peng, Z. Jiang, L. Zhu, Y. Wu, C. Xu, Z. Wang, M. Yang, H. Li, L. Chen and F. Wu, *Energy Storage Mater.*, 2024, **72**, 103749.
102 S. Lu, X. Zhang, Z. Yang, Y. Zhang, T. Yang, Z. Zhao, D. Mu and F. Wu, *Nano Lett.*, 2023, **23**, 10856–10863.
103 J. Zhou, S. Wang, C. Wu, J. Qi, H. Wan, S. Lai, T. W. Ko, Z. Liang, S. Feng, K. Zhou, N. Harpak, M. Liu, Z. Hui, P. J. Ai, H. Liu, W. Yan, Y. Ha, M.-J. Kim, K. Griffith, C. Wang, S. P. Ong and P. Liu, *Nano Lett.*, 2025, **25**, 12876–12883.
104 C. Zhao, L. Chen, Y. Che, Z. Pang, X. Wu, Y. Lu, H. Liu, G. M. Day and A. I. Copper, *Nat. Commun.*, 2021, **12**, 817.
105 Z. Lei, Y. Huang, Y. Zhu, D. Zhou, Y. Chen, S. Wang, W. Li, H. Li, X. Xi, Y. Liu, Y. Zhang, G. Zhang, X. Li, Q. Zhu, B. Zhang, S. Feng, S. Ye, W. Yan, S. Jiao, J. Jiang, M. Gu, R. Cao and Y. Luo, *J. Am. Chem. Soc.*, 2025, **147**, 21743–21753.
106 X. Yue, T. Song, J. Cao, X. Zhang, S. Feng, W. Shang, J. Jiang and L. Chen, *CCS Chem.*, 2025, DOI: 10.31635/ccschem.025.202505768.
107 Z. Li, M. Guo and W. Zhong, *Precis. Chem.*, 2025, **3**, 297–318.
108 Z. Hong and V. Viswanathan, *ACS Energy Lett.*, 2018, **3**(7), 1737–1743.